# Original Article

# Assessment of Maternal Heart-Rate Variability during Labor Using Wavelet-Based Power Spectral Analysis

Noritsugu Suzuki   Junichi Sugawara   Yoshitaka Kimura   Satoru Nagase
Kunihiro Okamura   Nobuo Yaegashi

Department of Obstetrics and Gynecology, Tohoku University Graduate School of Medicine, Sendai, Japan

## Abstract
*Objective:* Changes in the maternal cardiac autonomic nervous system were assessed in the presence and absence of uterine contractions by analyzing maternal heart-rate variability during labor using wavelet-based power spectral analysis. *Methods:* We assessed the heart-rate variability in 20 pregnant women during labor and in 15 pregnant women with threatened premature labor with the use of wavelet-based power spectral analysis. *Results:* There was no significant difference in high-frequency components between the uterine contraction and non-contraction periods. The intensities of the low-frequency and very-low-frequency components during uterine contractions were significantly stronger than the corresponding intensities between uterine contractions. *Conclusion:* Maternal sympathetic activity was upregulated during uterine contractions, and influenced the very-low-frequency components. This method of analysis may represent a novel means of identifying uterine contractions.                Copyright © 2012 S. Karger AG, Basel

## Introduction

Significant maternal hemodynamic changes occur in labor. During the first stage of labor in a normal pregnant woman, the basal cardiac output is increased by 12% in comparison to the pre-labor level. Cardiac output increases further during each contraction [1–3]. Each uterine contraction transfuses approximately 300–500 ml of blood from the uterine to the systemic circulation, which augments the stroke volume [4]. By the time complete cervical dilation is achieved, the intrapartum cardiac output has increased by 34% [5]. In addition to the hemodynamic changes associated with contractions, increased sympathetic activity resulting from pain and anxiety may also contribute to the increase in cardiac output [6]. Overall, it appears that maternal hemodynamics periodically change during labor and those changes may be modulated by temporal differences in the activity of the autonomic nervous system.

It is not possible to distinguish uterine contractions that lead to cervical dilation from those that do not, solely on the basis of a cardiotocogram. The uterine contractions associated with threatened premature labor (TPL) share a pattern with those associated with actual preterm labor. Therefore, a need exists for an alternative non-invasive means of assessing uterine contractions that distinguishes those leading to cervical dilation from those that do not.

It is plausible that TPL, by virtue of its lack of effect on cervical dilation, will not affect maternal hemodynamics in the same way as preterm labor that does produce cervical dilation. Therefore, monitoring changes in maternal hemodynamics may represent one way to assess what is taking place at the level of the cervix. One candidate parameter for monitoring is the maternal heart-rate variability (HRV).

HRV is affected by fluctuations in autonomic nervous system activity. Hales [7] first described this regulation in 1733. Variable bursts at the sinoatrial node are controlled by the sympathetic and parasympathetic branches of the autonomic nervous system. Power spectral analysis of HRV is one method of assessing autonomic nervous responses that has been previously validated in fetal lambs [8]. Conventional methods of spectral analysis employ a fast Fourier transformation [9]. Fast Fourier transformation analysis, however, is only appropriate for stationary signals [10]. Non-stationary signals, i.e. those in which the frequencies evolve with time, must be represented in a time-frequency plane. Time-frequency analysis using a wavelet transformation (WT) is a mathematical method suitable for the analysis of HRV [11]. With this transformation, global representative indexes of HRV have to be calculated as a set of cumulative spectrum powers contained in a given number of R-R intervals, which prevents temporal localization of sudden changes in the behavior of the R-R signal.

WT allows temporally localized sliding signal analysis to be performed, which gives the observer access at any time to the status of HRV, as, for example, when the balance of autonomic nervous system equilibrium is suddenly modified by acute clinical situations such as the onset of labor.

The purpose of this study was to assess maternal HRV during labor with use of wavelet-based power spectral analysis. Changes in maternal cardiac autonomic nervous system activity were correlated with the presence of uterine contractions. The goal of this study was to identify a potential non-invasive means of identifying contractions specifically associated with labor.

## Materials and Methods

Approval for this study was obtained in advance from the Ethical Commission on Research on Humans, School of Medicine of Tohoku University, Sendai, Japan. Informed consent was also obtained from each patient on a voluntary basis.

A total of 20 healthy pregnant women (gestational weeks 37–41, mean 39.5 ± 1.2) ranging in age from 21.9 to 40.5 years (mean 31.9 ± 5.2) with uncomplicated pregnancies were allocated to the labor group to evaluate the effect of uterine contractions on maternal autonomic nervous system activity. A total of 15 pregnant women with TPL (gestational weeks 31–34, mean 32.7 ± 1.2) ranging in age from 21.9 to 40.5 years (mean 31.9 ± 5.2) were allocated to the TPL group. None of the subjects had hypertension, diabetes, heart disease, or any other diagnosed medical condition complicating the pregnancy. All women had appropriately grown fetuses for the gestational age. Pregnant women in the TPL group had uterine contractions more often than twice per 20 min. We excluded women from the TPL group if they experienced pain with the contractions. Additionally, women who reported being anxious were excluded as anxiety is a known modulator of the autonomic nervous system.

We assessed pregnant women in the labor group on an off-line basis, obtaining HRV data for 20 min starting from 30 min before the expected time of delivery; data were obtained for women in the TPL group for a 20-min period without administration of any medication that could affect heart rate. The electrocardiogram (ECG) was monitored using a triple-wire cable with electrodes (BSM-9510; Nihon-Kohden, Japan) attached at standard unipolar chest positions. Uterine contractions were externally monitored from the abdominal skin surface of each pregnant woman using a tocotransducer (Trimline; Corometrics Medical Systems, Inc., Conn., USA). A limitation of the external monitoring system was that it was not possible to identify the true points of increase in intrauterine pressure; however, for the purposes we defined the period of a uterine contraction and the period between contractions based on cardiotocography charts. We performed the spectral analysis for 1-min intervals in both the contraction and non-contraction periods. We digitally stored the data for electric voltage of the ECG lead II and the uterine tocogram continuously and simultaneously.

The RR intervals (to the millisecond) were extracted from the ECG data and the corresponding time intervals sampled from the cardiotocogram with an accuracy of 0.25 s. In the spectral analysis of maternal HRV, we identified three definite frequency bands and classified them into high frequency (HF, 0.15–0.4 Hz), low frequency (LF, 0.04–0.15 Hz), and very low frequency (VLF, –0.04 Hz) with the same definitions as those used by the Task Force of the European Society of Cardiology and the North American Society of Pacing and Electrophysiology [12]. All data manipulation and analysis were performed using software developed by our group. We used our software in accordance with Y. Ishikawa's theory (Wavelet Analysis and Spectrum Analysis Software: MEM; Igaku-Shuppan, Tokyo, Japan) to carry out the wavelet analysis.

In terms of the WT, we refer readers to the study by Ivanov et al. [13]. WT has been used to analyze observed biological signals including human HRV since 1996 [13]. WT is usually devoted to the analysis of non-stationary signals. There are no prerequisites regarding the stability of the frequency content of the signal to be analyzed. Decomposition of a signal requires designation of a 'mother wavelet.' A mother wavelet slides along the time direction and contracts or stretches in the heart-rate region. This enables a three-dimensional or contour plot to be obtained, allowing changes in the dominant frequency range over time to be observed. Further details on WT have been published elsewhere [13, 14]. For the mother wavelet we chose 'Morlet power,' which was

Junichi Sugawara, MD
Department of Obstetrics and Gynecology
Tohoku University Graduate School of Medicine
1-1, Seiryomachi, Aobaku, Sendai 980-8574 (Japan)
Tel. +81 22 717 7251, E-Mail jsugawara@med.tohoku.ac.jp

established by Morlet et al. [15, 16] to analyze the electrocardiography-deforming Gauss function.

The spectral intensity in each frequency band was evaluated with WT for 20 min. We compared values obtained during a labor contraction with those obtained between contractions, and averaged the intensity of each component during the two periods. Statistical comparison was performed by Wilcoxon signed-rank test and differences were significant at p < 0.05. Each value is expressed as the mean ± SE.

## Results

An example of the analysis of the maternal HR is displayed in figure 1.

Figure 2 demonstrates the spectral intensity of the HF, LF, and VLF components of maternal HRV in the uterine contraction and non-contraction periods for women in the labor group. There was no significant difference in HF components between the uterine contraction and non-contraction time periods. The intensities of the LF and VLF components were significantly stronger in the uterine contraction period than in the non-contraction period (p < 0.001).

Figure 3 demonstrates the spectral intensities of the HF, LF, and VLF components of maternal HRV in uterine contraction and non-contraction periods for women in the TPL group. There were no significant differences in the HF components between the uterine contraction and non-contraction time periods. In contrast, the intensities of the LF and VLF components were significantly higher in the uterine contraction period than in the non-contraction period (p < 0.01 and p < 0.001, respectively).

Figure 4 demonstrates the ratio of LF/HF components of maternal HRV in the uterine contraction and non-contraction periods for women in the labor group and the TPL group. There was a significant difference in the ratios seen in both the contraction and non-contraction periods between the two groups (p < 0.05).

## Discussion

Using time-frequency analysis, the present study clearly demonstrated dynamic changes in maternal HRV during labor. We observed that the LF and VLF components were significantly higher in intensity during a contraction than they were between uterine contractions, whereas the HF component did not show any changes.

Since the initial report of Wolf et al. [17], different methodologies have been developed to measure HRV
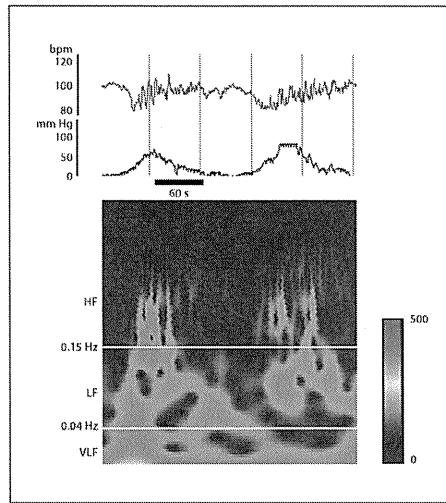
components in experimental and clinical settings [18]. Vagal activity is the major contributor to the HF component, as demonstrated by observed changes in heart rate following vagal stimulation, administration of muscarinic receptor antagonists, or vagotomy [19, 20]. In contrast, the data regarding the LF component are conflicting. Some studies [21–24] suggest that the LF component is a quantitative marker of sympathetic modulation, whereas other studies suggest that it reflects both sympathetic and vagal activity [19, 25]. The LF/HF ratio has been proposed as an index of sympatho-vagal interaction to explore the autonomic control of the sinoatrial node [21].

Our finding of no significant difference in HF intensity between the uterine contraction period and the non-contraction period implies there is no obvious change in maternal vagal activity during labor. Two possibilities should be considered for the mechanism underlying the upregulation of the LF component during a uterine contraction: one is that sympathetic activity alone is facilitated during uterine contractions, and the other is that both sympathetic and parasympathetic activities are augmented during uterine contraction. If we consider the HF
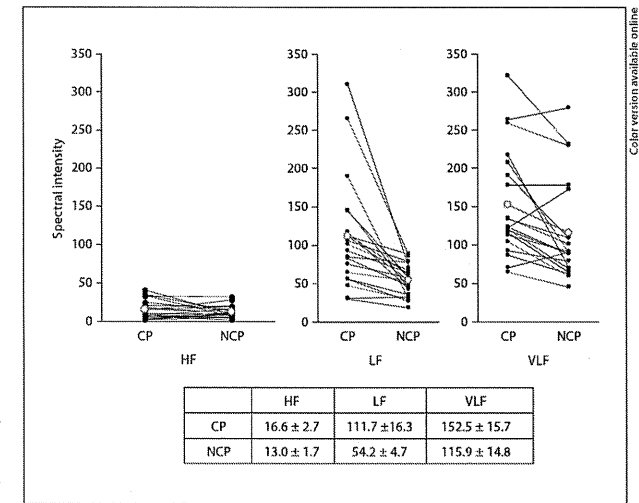


**Fig. 1.** An example of the analysis of maternal heart rate, uterine contraction, and the time-dependent spectrum of HR.



**Fig. 2.** Spectral intensity of each component of variability in women in the labor group (mean ± SE). CP = Contraction period; NCP = non-contraction period. HF = high frequency; LF = low frequency; VLF = very low frequency.
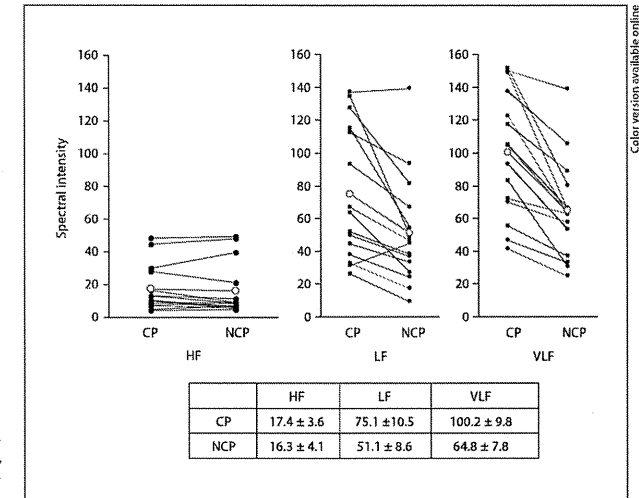
|  | HF | LF | VLF |
|---|---|---|---|
| CP | 16.6 ± 2.7 | 111.7 ± 16.3 | 152.5 ± 15.7 |
| NCP | 13.0 ± 1.7 | 54.2 ± 4.7 | 115.9 ± 14.8 |



**Fig. 3.** Spectral intensity of each component of variability in women in the TPL group (mean ± SE). Abbreviations as explained in figure 2.

|  | HF | LF | VLF |
|---|---|---|---|
| CP | 17.4 ± 3.6 | 75.1 ± 10.5 | 100.2 ± 9.8 |
| NCP | 16.3 ± 4.1 | 51.1 ± 8.6 | 64.8 ± 7.8 |

238

component a reflection of the vagal tone in the mother that is not augmented during a uterine contraction, elevation of the LF component during the uterine contraction would mainly be induced by the upregulated sympathetic activity. The current literature supports the view that the LF component reflects at least sympathetic input to the heart and the activity of chemo- and baroreceptors [21, 26].

Pain and anxiety associated with labor may contribute to 50–60% of the increase in labor-related changes in cardiac output [6, 27]. Stress such as pain or anxiety accelerates the secretion of catecholamines released from the sympathetic ganglion, which augments sympathetic activity. The levels of plasma catecholamines in patients who have elective cesarean sections have been demonstrated to be significantly lower than levels in women who have a vaginal delivery [28]. In addition, the maternal epinephrine concentration during uterine contractions is higher than that measured between contractions [29]. The increase of the LF component during uterine contractions is probably induced by catecholamine increase. It may also be associated with maternal labor pain and anxiety, which increase heart rate and blood pressure via sympathetic pathways.

Uterine contractions during labor transfuse approximately 300–500 ml blood from the uterine to maternal circulation [4]. In general, intravenous fluid infusion to increase the maternal blood volume stimulates the Bainbridge reflex and increases cardiac output with an increase in heart rate. Increased cardiac output in turn elevates the blood pressure. Likewise, in a uterine contraction, transfused blood from the uterus increases the heart rate and blood pressure. The increase in heart rate and blood pressure then activates baroreceptors thereby increasing the LF component, which reflects baroreceptor activity.

The pregnant women in the TPL group had uterine contractions, which were painless. In this case, the increase in the intensity of the LF component was more a reflection of autotransfusion rather than pain or anxiety-induced sympathetic activity.

The VLF component is the least understood of the three components – it is thought to be associated with thermoregulatory feedback mechanisms [30], renin-angiotensin activity [19], and circulating neurohormone levels [26]. Recently, Taylor et al. [31] revealed that atropine nearly abolished the VLF components and concluded that the parasympathetic nervous system is the dominant determinant of the VLF component. In this study, the VLF components of women in the TPL group in-
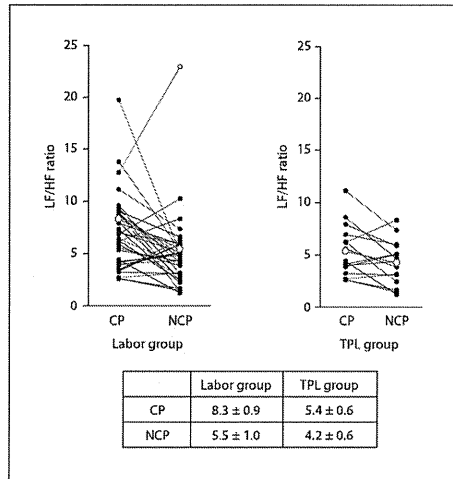


**Fig. 4.** LF/HF ratio contraction and non-contraction periods in the labor and TPL groups (mean ± SE). Abbreviations as explained in figure 2.

creased during the uterine contractions, which were painless. It is plausible that the VLF component may respond to blood volume changes as in autotransfusion. Vagal activity probably did not influence the VLF component as it did not vary in parallel with the HF component.

In summary, the use of time-frequency analysis of maternal HRV during labor allowed us to clarify that the LF and VLF components during a uterine contraction are significantly higher than they are between contractions: this implies relative upregulation of the sympathetic nervous system during uterine contractions. This is the first observation of maternal autonomic nervous system activity measured non-invasively across uterine contractions. This technique may improve the understanding of the maternal physiological adaptations during labor. Additionally, this technique may, with further refinement, provide a novel means by which to diagnose abnormal contraction states including preterm labor.

## References

1 Ueland K, Hansen JM: Maternal cardiovascular dynamics. Labor and delivery under local and caudal analgesia. Am J Obstet Gynecol 1969;103:8–18.
2 Kjeldsen J: Hemodynamic investigations during labour and delivery. Acta Obstet Gynecol Scand Suppl 1979;89:1–252.
3 Robson SC, Dunlop W, Boys RJ, Hunter S: Cardiac output during labour. Br Med J (Clin Res Ed) 1987;295:1169–1172.
4 Lee W, Rokey R, Miller J, Cotton DB: Maternal hemodynamic effects of uterine contractions by M-mode and pulsed-Doppler echocardiography. Am J Obstet Gynecol 1989; 161:974–977.
5 Hunter S, Robson SC: Adaptation of the maternal heart in pregnancy. Br Heart J 1992; 68:540–543.
6 Henricks CH, Quilligna EJ: Cardiac output during labor. Am J Obstet Gynecol 1956;71: 953–972.
7 Hales S: Statistical essays; in Haemastaticks. London, Innings & Manby, 1733.
8 Kimura Y, Okamura K, Watanabe T, Murotsuki J, Suzuki T, Yano M, Yajima A: Power spectral analysis for autonomic influences in heart rate and blood pressure variability in fetal lambs. Am J Physiol 1996;271:H1333–H1339.
9 Divon MY, Winkler II, Yeh SY, Platt LD, Langer O, Merkatz IR: Diminished respiratory sinus arrhythmia in asphyxiated term infants. Am J Obstet Gynecol 1986;155: 1263–1266.
10 Chaffin DG, Goldberg CC, Reed KL: The dimension of chaos in the fetal heart rate. Am J Obstet Gynecol 1991;165:1425–1429.
11 Kimura Y, Okamura K, Watanabe T, Yaegashi N, Uehara S, Yajima A: Time-frequency analysis of fetal heartbeat fluctuation using wavelet transform. Am J Physiol 1998; 275:H1993–H1999.
12 Task Force of the European Society of Cardiology and the North American Society of Pacing and Electrophysiology: Heart rate variability: standards of measurement, physiological interpretation and clinical use. Circulation 1996;93:1043–1065.

13 Ivanov PC, Rosenblum MG, Peng CK, Mietus J, Havlin S, Stanley HE, Goldberger AL: Scaling behaviour of heartbeat intervals obtained by wavelet-based time-series analysis. Nature 1996;383:323–327.
14 Pichot V, Gaspoz JM, Molliex S, Antoniadis A, Busso T, Roche F, Costes F, Quintin L, Lacour JR, Barthelemy JC: Wavelet transform to quantify heart rate variability and to assess its instantaneous changes. J Appl Physiol 1999;86:1081–1091.
15 Morlet D, Peyrin F, Desseigne P, Touboul P, Rubel P: Wavelet analysis of high-resolution signal-averaged ECGs in postinfarction patients. J Electrocardiol 1993;26:311–320.
16 Morlet D, Couderc JP, Touboul P, Rubel P: Wavelet analysis of high-resolution ECGs in post-infarction patients: role of the basic wavelet and of the analyzed lead. Int J Biomed Comput 1995;39:311–325.
17 Wolf MM, Varigos GA, Hunt D, Sloman JG: Sinus arrhythmia in acute myocardial infarction. Med J Aust 1978;15:52–53.
18 Task Force of the European Society of Cardiology and the North American Society of Pacing and Electrophysiology: Heart rate variability: standards of measurement, physiological interpretation, and clinical use. Eur Heart J 1996;17:354–381.
19 Akselrod S, Gordon D, Ubel FA, Shannon DC, Barger AC, Cohen RJ: Power spectrum analysis of heart rate fluctuation: a quantitative probe of beat to beat cardiovascular control. Science 1981;213:220–222.
20 Pomeranz M, Macaulay RJ, Caudill MA, Kutz I, Adam D, Gordon D, Kilborn KM, Barger AC, Shannon DC, Cohen RJ, Benson M: Assessment of autonomic function in humans by heart rate spectral analysis. Am J Physiol 1985;248:H151–H153.

21 Malliani A, Pagani M, Lombardi F, Cerutti S: Cardiovascular neural regulation explored in the frequency domain. Circulation 1991;84:482–492.
22 Cerati D, Schwartz PJ: Single cardiac vagal fiber activity, acute myocardial ischemia, and risk for sudden death. Circ Res 1991;69: 1389–1401.
23 Kamath MV, Fallen EL: Power spectral analysis of heart rate variability: a noninvasive signature of cardiac autonomic function. Crit Rev Biomed Eng 1993;21;245–311.
24 Rimoldi O, Pierini S, Ferrari A, Cerutti S, Pagani M, Malliani A: Analysis of short-term oscillations of R-R and arterial pressure in conscious dogs. Am J Physiol 1990; 258:H967–H976.
25 Appel ML, Berger RD, Saul JP, Smith JM, Cohen RJ: Beat to beat variability in cardiovascular variables: noise or music? J Am Coll Cardiol 1989;14:1139–1148.
26 Saul JP: Beat-to-beat variations of heart rate reflect modulation of cardiac autonomic outflow. NIPS 1990;5:32–37.
27 Elkayam U, Gleicher N: Hemodynamic and cardiac function during normal pregnancy and the puerperium; in Elkayam U, Gleicher N (eds): Cardiac Problems in Pregnancy. New York, Wiley-Liss, 1998, pp 3–19.
28 Wang L, Zhang W, Zhao Y: The study of maternal and fetal plasma catecholamine levels during pregnancy and delivery. J Perinat Med 1999;27:195–198.
29 Alchagen S, Wijma K, Lundberg U, Melin B, Wijma B: Catecholamine and cortisol reaction to childbirth. Int J Behav Med 2001;8: 50–65.
30 Hyndman BW, Kitney RI, Sayers BM: Spontaneous rhythms in physiological control systems. Nature 1971;233:339–341.
31 Taylor JA, Carr DL, Myers CW, Eckberg DL: Mechanisms underlying very-low-frequency RR-interval oscillations in humans. Circulation 1998;98:547–555.

# Time-varying inter-hemispheric coherence during corpus callosotomy

CrossMark

Eiichi Okumura [a], Masaki Iwasaki [b,*], Rie Sakuraba [a], Izumi Itabashi [a], Shin-ichiro Osawa [b], Kazutaka Jin [a], Hisashi Itabashi [a], Kazuhiro Kato [a], Akitake Kanno [c], Teiji Tominaga [b], Nobukazu Nakasato [a]

[a] Department of Epileptology, Tohoku University School of Medicine, Sendai, Miyagi, Japan
[b] Department of Neurosurgery, Tohoku University School of Medicine, Sendai, Miyagi, Japan
[c] Department of Functional Brain Imaging, Institute of Development, Aging and Cancer, Tohoku University, Sendai, Japan

## ARTICLE INFO

## HIGHLIGHTS

- Inter-hemispheric coherence is decreased during the final stage of corpus callosotomy and the effect is maximized after sectioning is completed.
- Various patterns of coherence decrease suggest individual variations in the participation of the corpus callosum in the genesis of bilateral synchrony.
- Intra-operative monitoring of inter-hemispheric EEG coherence with wavelet transform coherence and trend analysis techniques is useful to estimate the physiological completeness of callosal sectioning.

## ABSTRACT

*Objective:* Corpus callosotomy limits the bilateral synchrony of epileptic discharges. However, the instantaneous changes in bilateral synchrony during corpus callosotomy are unclear. The present study investigated how and when bilateral synchrony is suppressed in the anterior and then posterior steps of corpus callosotomy.
*Methods:* Intra-operative scalp electroencephalography (EEG) was recorded simultaneously with surgical video for six patients who underwent total corpus callosotomy for medically intractable drop attacks. The time-varying EEG inter-hemispheric coherence was quantified by wavelet transform coherence and trend analysis.
*Results:* The 4–13 Hz coherence decreased after corpus callosotomy in five patients. Significant decrease in coherence was observed only during the posterior step of callosal sectioning in three patients, but throughout both steps in two patients.
*Conclusions:* Decrease in inter-hemispheric coherence is not always correlated with the stages of callosal sectioning. Inter-hemispheric coherence is decreased during the final stage of corpus callosotomy and the effect is maximized after sectioning is completed.
*Significance:* Various patterns of coherence decrease suggest individual variations in the participation of the corpus callosum in the genesis of bilateral synchrony. Time-varying inter-hemispheric EEG coherence is useful to monitor the physiological completeness of corpus callosotomy.
© 2013 International Federation of Clinical Neurophysiology. Published by Elsevier Ireland Ltd. All rights reserved.

## 1. Introduction

Corpus callosotomy is a palliative surgical procedure for patients with medically intractable seizures who are not candidates for focal resection (Asadi-Pooya et al., 2008). The corpus callosum is the most important pathway for inter-hemispheric spread of epileptic activity and the major anatomical substratum for seizure bilateralization and bisynchronization (Lemieux and Blume, 1986; Wada, 1995). Callosal connections are broadly distributed over roughly 70–80% of the cortex (Kaas, 1995), and most are connected to homologous areas in the opposite hemisphere (Waxman, 2003). The cortex generates inhibitory and excitatory activities that are balanced by the corpus callosum (Musiek, 1986).

The physiological purpose of corpus callosotomy is to suppress bilateral synchrony. Various studies have compared epileptiform discharges, i.e., interictal spikes and/or sharp waves, before and

* Corresponding author. Address: Department of Neurosurgery, Tohoku University Graduate School of Medicine, 1-1 Seiryo-machi, Aoba-ku, Sendai, Miyagi 980-8574, Japan. Tel.: +81 22 717 7230; fax: +81 22 717 7233.
E-mail address: epinetmi@gmail.com (M. Iwasaki).

**Table 1**
Clinical characteristics of the 6 patients.

| Case No. | Age (year)/sex | Etiology of epilepsy | Semiology | EEG spikes | | Seizure outcome | |
|---|---|---|---|---|---|---|---|
| | | | | Pre-operative | Post-operative | Drop attacks | Other seizure types |
| 1 | 7/M | Tuberous sclerosis complex | Axial tonic seizure | Generalized slow spike wave complexes | Lt and Rt hemisphere spikes | No changes | No changes |
| 2 | 2/M | Down syndrome (21 trisomy) | Spasm | Generalized and multifocal spikes | Generalized spikes, Rt and Lt hemisphere spikes | >90% reduction | >50% Reduction |
| 3 | 9/F | Viral encephalitis | Axial tonic seizure | Generalized spikes, Rt and Lt frontal spikes | Generalized spikes, Rt hemisphere spikes | Free | >75% Reduction |
| 4 | 3/M | Tuberous sclerosis complex | Axial tonic seizure | Multifocal spikes | Lt temporo-occipital spikes | Free | >75% Reduction |
| 5 | 31/F | Unknown | Axial tonic seizure | Generalized and multifocal spikes | Not performed | Free | >90% Reduction |
| 6 | 5/M | Ischemic brain injury of Lt hemisphere | Axial tonic seizure | Rt and Lt hemisphere spikes | Rt hemisphere and Lt occipital spikes | Free | >90% Reduction |

after corpus callosotomy (Spencer et al., 1993; Oguni et al., 1994; Quattrini et al., 1997; Matsuzaka et al., 1999; Clarke et al., 2007; Iwasaki et al., 2011). Long-term scalp electroencephalography (EEG) monitoring has demonstrated reduction of epileptiform discharges in both hemispheres after corpus callosotomy, suggesting that callosal connections facilitated the asymmetrically epileptogenic hemispheres to develop bisynchronous and bisymmetrical epileptiform discharges (Matsuo et al., 2003). Little has been reported on the real-time EEG change during sequential steps of corpus callosotomy. Lateralization or blockade of bisynchronous epileptiform discharges were observed intra-operatively after callosal section (Fiol et al., 1993; Lin and Kwan, 2012). EEG changes were analyzed by visual inspection, and correlation of post-operative seizure outcome attempted. Studies of inter-hemispheric connections are of special importance, and callosal connections are testable with noninvasive EEG in humans (Thatcher et al., 1986; Montplaisir et al., 1990; Pinkofsky et al., 1997; Knyazeva and Innocenti, 2001). However, no quantitative measures for inter-hemispheric coherence have been implemented previously for monitoring EEG during corpus callosotomy.

We hypothesized that monitoring of instantaneous EEG changes during corpus callosotomy could provide a predictor for post-operative outcome. The present study investigated the modulation of inter-hemispheric EEG coherence in the different stages of corpus callosotomy.

## 2. Methods

### 2.1. Subjects

This study included 6 consecutive patients with drug-resistant symptomatic generalized epilepsy who underwent total corpus callosotomy for alleviation of "drop attacks." The clinical characteristics are summarized in Table 1. The etiology was symptomatic in 5 patients and unknown in one. All patients except one (Case 6) were diagnosed with West syndrome at the time of onset of epilepsy. All patients had epileptic seizures intractable to available medical therapies. Drop attacks due to sudden tonic or atonic seizures occurred as one of their main seizure types. Median post-operative follow-up period was 6 months, ranging from 1 to 12 months. The Ethics Committee of Tohoku University Graduate School of Medicine approved this study.

### 2.2. EEG recording during total callosotomy procedures

Intra-operative EEG during corpus callosotomy was recorded using scalp electrodes attached to 14 locations of the international
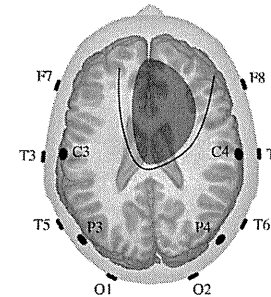


Fig. 1. Scalp electrode placement and operative field. Skin incision (black line) and area of craniotomy (gray) are illustrated for the right-side approach. The nomenclature is based on the international 10–20 system of scalp electroencephalography.
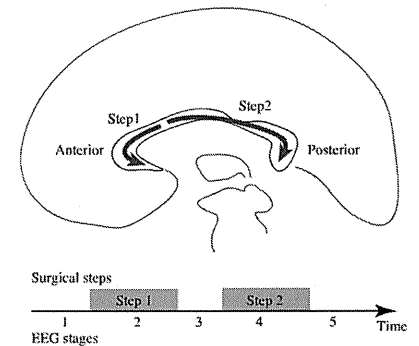


Fig. 2. Procedural steps of corpus callosotomy and EEG staging. Callosal sectioning was started at the midline approximately 2 cm posterior to the genu of the corpus callosum. The anterior part including the genu and rostrum was first dissected anteriorly (Step 1), and then the posterior part including the isthmus and splenium was dissected posteriorly (Step 2). Stage 2 extends from the start to the end of anterior corpus callosotomy, and Stage 4 from the start to the end of posterior corpus callosotomy.

10–20 system (F7/8, T3/4, C3/4, P3/4, T5/6, O1/2, and A1/2 shown in Fig. 1) outside the operative field. EEG data were sampled at 1000 Hz after band-pass filtering of 0.08 and 300 Hz (EEG-2100; Nihon-Koden Co., Tokyo, Japan). Video from the operating microscope was simultaneously recorded to correlate the timing of EEG and surgical procedures.

### 2.3. Corpus callosotomy and stages of scalp EEG monitoring

Total corpus callosotomy was performed through right or left paramedian frontal craniotomy. Sectioning of the corpus callosum was divided into two major steps. In brief, callosal sectioning was started at the midline approximately 2 cm posterior to the genu of the corpus callosum. The anterior part including the genu and rostrum was first dissected anteriorly (Step 1), and then the posterior part including the isthmus and splenium was dissected posteriorly (Step 2) (Fig. 2). The details of the surgery were described elsewhere (Iwasaki et al., 2012). All surgical procedures were performed by the same author (MI). Sevoflurane was used in combination with remifentanil for anesthesis during the surgery for all patients. The end-tidal sevoflurane concentration was maintained at a constant level between 1.3% and 2.5%.

The attending neurosurgeon (MI) retrospectively defined 5 different stages of scalp EEG, based on the simultaneously recorded surgical video, as follows: before (Stage 1) and during (Stage 2) Step 1 of callosal sectioning; before (Stage 3), during (Stage 4), and after (Stage 5) Step 2 of callosal sectioning (Fig. 2).

### 2.4. Data analysis

#### 2.4.1. Conventional review of scalp EEG

To evaluate the relationship between the frequency of epileptic spikes and changes in bilateral coherence, two EEG technicians (RS and II) reviewed all EEG recordings on the longitudinal bipolar montage, and manually marked the peaks of all epileptic spikes. The marked peaks were further reviewed by a board-certified physician of clinical neurophysiology (MI). The frequency of epileptic spikes was calculated for each EEG stage. The spike frequencies per minute were compared between before (Stage 1) and after (Stage 5) corpus callosotomy with the paired t-test.

#### 2.4.2. Preprocessing

A band-stop filter was applied to remove line noise (50 Hz and harmonics) caused by the power supply. Segments containing any artifacts (e.g., due to bipolar electronic cautery) were excluded from further analysis on the basis of criteria (±50 μV) for high frequency (more than 50 Hz) components of the data. For the following instantaneous functional connectivity analysis, continuous EEG data were band-pass filtered from 1.0 to 100 Hz, downsampled to 200 Hz, and extracted from 10 min before to 10 min after callosotomy.

#### 2.4.3. Functional connectivity analysis: wavelet transform coherence

To evaluate the functional connectivity between the two EEG time series, wavelet transform coherence (WTC) was used. WTC is a method for analyzing the instantaneous coherence and phase lag between two time series as a function of both time and frequency (Torrence and Compo, 1998), and is therefore well suited to investigating nonstationary changes (Chang and Glover, 2010) in coupling between intra-operative EEG time series.

WTC is based on the continuous wavelet transform, which decomposes a single time series into time–frequency space by successively convolving the time series with scaled and translated versions of a wavelet function $\psi_0$ (Mallat, 1999). The continuous wavelet transform of a time series $x_n$ of length $N$, sampled from an underlying continuous waveform at equal time steps of size $\Delta t$, is defined as:

$$W^X(n,s) = \sqrt{\frac{\Delta t}{s}}\sum_{n'=1}^{N} x_{n'}\psi_0\left[(n'-n)\left(\frac{\Delta t}{s}\right)\right] \quad (1)$$

where $n$ is a time index and $s$ denotes the wavelet scale. The function is $\psi_0$ chosen to be the complex Morlet wavelet:

$$\psi_0(\eta) = \pi^{-1/4}e^{i\omega_0\eta}e^{-\eta^2/2}$$

where the parameter $\omega_0$ governs the relative time and frequency resolution; here, $\omega_0 = 6$, which has been shown to provide a good trade-off between time and frequency localization (Grinsted et al., 2004; Muller et al., 2004). For the Morlet wavelet with $\omega_0 = 6$ the Fourier period ($T$) associated with scale $s$ is approximately equal to the value of $s$ ($T = 1.03s$). Note that $\psi_0$ is normalized to unit energy at each scale in Eq. (1), so that the wavelet transforms at each scale are directly comparable.

The wavelet transform $W^X(n,s)$ is a complex quantity whose modulus, wavelet power $|W^X(n,s)|$, expresses the amount of power in $x$ as a function of time and frequency (scale), and whose angle represents the local phase. Similarly, the cross-wavelet transform can be defined for two time series as:

$$W^{XY}(n,s) = W^X(n,s)W^{Y*}(n,s) \quad (2)$$

where * denotes complex conjugation. The modulus of Eq. (2), $|W^{XY}(n,s)|$, known as the cross-wavelet power, expresses the amount of joint power between $x$ and $y$ as a function of time and frequency, and whose angle (cross-wavelet phase) describes their relative phase. Following (Torrence and Webster, 1999), the wavelet transform coherence is defined as

$$R^2(n,s) = \frac{\left|\langle s^{-1}W^{XY}(n,s)\rangle\right|^2}{\left|\langle s^{-1}W^X(n,s)\rangle\right|^2\left|\langle s^{-1}W^Y(n,s)\rangle\right|^2}$$

which reveals localized regions of phase-locked behavior. $R^2$ ranges between 0 and 1, and can be conceptualized as a localized correlation coefficient in time and frequency space (Grinsted et al., 2004). The brackets $\langle\rangle$ indicate smoothing in both time and scale: the filter for temporal smoothing is a Gaussian function, which is matched to the Morlet wavelet (Torrence and Webster, 1999).

The statistical significance of WTC magnitude was estimated using a Monte Carlo approach. An autoregressive process was fitted to each input pair of the time series ($x$ and $y$), and a large number (here, 1000) of bootstrapped time series pairs with the same AR coefficients and model order as $x$ and $y$ were generated. For each bootstrapped pair, the WTC could be calculated and a null distribution estimated for each scale, from which significance levels were derived.

To evaluate the inter-hemispheric connectives, the homotopic combinations of electrodes were defined as the following five pairs: F7–T3 and F8–T4 (FT), T3–T5 and T4–T6 (T), T5–O1 and T6–O2 (TO), C3–P3 and C4–P4 (CP), P3–O1 and P4–O2 (PO).

#### 2.4.4. Comparison of coherence immediately before (Stage 1) and after (Stage 5) callosal sectioning

To reveal the pre-operative and post-operative characteristics of inter-hemispheric coherence, the differences in means were evaluated between stage-averaged WTCs for Stage 1 and Stage 5 using a paired t-test. First, the WTC spectra were converted to Fisher's Z-transformed coherence values (Nolte et al., 2004) and averaged across the specified frequency band. Next, this band-averaged WTC was averaged across segments with 1-min steps. Finally, the WTC data of Stage 1 and Stage 5 were compared using a paired t-test. Raw p values were corrected for multiple comparisons using the false discovery rate (FDR) approach (Genovese et al., 2002), and these corrected p values were used in all statistical tests.

**Table 2**
Operative durations of callosal sectioning and the frequency of spikes.

| Case No. | Durations (min) | | Number of spikes | | Spike frequency (spikes per min) | |
|---|---|---|---|---|---|---|
| | Stage 2 | Stage 4 | Stage 2 | Stage 4 | Stage 2 | Stage 4 |
| 1 | 17.7 | 14.0 | 526 | 500 | 29.7 | 35.6 |
| 2 | 17.6 | 12.8 | 158 | 76 | 9.0 | 6.0 |
| 3 | 12.2 | 20.9 | 293 | 607 | 24.0 | 29.0 |
| 4 | 14.3 | 21.0 | 24 | 75 | 1.7 | 3.6 |
| 5 | 16.6 | 63.9 | 25 | 52 | 1.5 | 0.8 |
| 6 | 38.2 | 14.3 | 1932 | 594 | 50.6 | 41.7 |

#### 2.4.5. Trend analysis

To reveal the time-varying characteristics of inter-hemispheric coherence during different stages of callosal section, the presence of significant temporal changes was evaluated using the non-parametric trend analysis (Mann–Kendall test and Sen's slope estimator techniques) and Spearman's rank correlation coefficient.

The Mann–Kendall test is a signed rank test for identifying trends in time series data (Kendall, 1938). The test compares the relative magnitudes of sample data rather than the data values themselves. One advantage of this test is that the data need not conform to any particular distribution. The second advantage of the test is the low sensitivity to abrupt breaks due to inhomogeneous time series (Jaagus, 2006). The Mann–Kendall test was applied by considering the statistic $S$ as:

$$S = \sum_{k=1}^{n-1}\sum_{j=k+1}^{n}\text{sgn}(x_j - x_k)$$

$$\text{sgn}(x_j - x_k) = \begin{cases} +1 & \text{if } (x_j - x_k) > 0 \\ 0 & \text{if } (x_j - x_k) = 0 \\ -1 & \text{if } (x_j - x_k) < 0 \end{cases}$$

where the $x_j$ are the sequential data values, $n$ is the length of the time-series. The mean $E[S] = 0$ and variance $Var[S]$ of the statistic $S$ were obtained as:

$$Var[S] = \frac{n(n-1)(2n+5) - \sum_t t(t-1)(2t+5)}{18}$$

The notation $t$ is the extent of any given tie and $\sum_t$ denotes the summation over all ties. In cases $t$ where the sample size $n > 10$, the standard normal variable $Z_{MK}$ is calculated by:

$$Z_{MK} = \begin{cases} \frac{S-1}{\sqrt{Var[S]}} & \text{if } S > 0 \\ 0 & S = 0 \\ \frac{S-1}{\sqrt{Var[S]}} & \text{if } S < 0 \end{cases}$$

Positive values of $Z_{MK}$ indicate increasing trends whereas negative values of $Z_{MK}$ indicate decreasing trends. When testing either increasing or decreasing monotonic trends at a $p$ significance level, the null hypothesis was rejected for absolute value of $Z_{MK}$ greater than $Z_{1-p/2}$, obtained from the standard normal cumulative distribution tables.

If a linear trend is present in a time series, then the true slope (change per unit time) can be estimated by using a simple non-parametric procedure (Sen, 1968). The slope estimates of $N$ pairs of data are first calculated by

$$Q_i = \frac{x_j - x_k}{j-k} \text{ for } i = 1,...,N, \quad j > k$$

where $x_j$ and $x_k$ are data values at times $j$ and $k$, respectively. If there are $n$ values $x_j$ in the time series, the same number of

$N = n(n-1)/2$ slope estimates $Q_i$ are obtained. The Sen's estimator of slope is the median of these $N$ values of $Q_i$. The $N$ values of $Q_i$ are ranked from the smallest to the largest and the Sen's estimator is

$$Q = \begin{cases} Q_{\frac{N+1}{2}} & \text{if } N \text{ is odd} \\ \frac{1}{2}(Q_{\frac{N}{2}} + Q_{\frac{N+1}{2}}) & \text{if } N \text{ is even} \end{cases}$$

Finally, a $100(1-\alpha)\%$ two-sided confidence interval of the slope estimate is obtained by the non-parametric technique based on the normal distribution.

To evaluate either long-term or short-term temporal drift, the statistical tests were performed using the following algorithm. First, the segment width to apply the trend analysis was defined as the whole time of WTC data. The WTC trend data were calculated by averaging across the time windows of the segment width. This averaging was performed on Fisher's Z-transformed coherence values. Next, the previous segment width was divided into halves, and the trend analysis was performed for the new segments defined as continuously moving in steps of 75% overlap. This algorithm was reiterated until the segment width became less than 5 min.

### 2.5. Implementation

All data analyses were performed in MATLAB® 7.14 (Math-Works, Inc., Natick, MA, USA) using custom scripts. The spectral filtering was implemented using the FIR1 command of Signal Processing Toolbox™ 6.17 (MathWorks, Inc.).

WTC was implemented using a library of MATLAB functions (Revision 16, February 6, 2008) provided by Grinsted et al. (2004) (http://www.pol.ac.uk/home/research/waveletcoherence/). Spearman's rank correlation coefficient and paired t-test were implemented using Statistics Toolbox™ 8.0 (MathWorks, Inc.). The Mann–Kendall test and the Sen's slope estimator were run using the MATLAB code "Mann–Kendall Tau-b with Sen's Method (enhanced)" provided by Jeff Burkey through the MATLAB Central file exchange (http://www.mathworks.com/matlabcentral/fileexchange/11190, accessed August 2012).

### 3. Results

Total sectioning of the corpus callosum was completed as described in the method without complications in all cases. The durations required for the anterior and posterior steps of callosotomy and the frequency of epileptic spikes are summarized in Table 2. No significant changes were observed in the average frequency of epileptic spikes between before (Stage 1) and after (Stage 5) corpus callosotomy ($p < 0.05$).

#### 3.1. WTC

The WTC spectrum of Case 1 (Fig. 3a) shows that WTC was abruptly decreased during the last step of corpus callosotomy (Stage 4) on all channel pairs. The averaged WTC of each stage shown in Fig. 3b indicated that the frequency range of 4–13 Hz is seemed to be dominant for Case 1. The dominant frequency range was similar for the other patients, so we focused on the range 4–13 Hz for further trend analysis.

#### 3.2. Comparison of pre-operative and post-operative coherence (Stage 1 vs. Stage 5)

WTC generally ranged from 0.8 to 0.9 with remarkable fluctuations. The 4–13 Hz WTC decreased after corpus callosotomy in a subset of channel pairs in five patients (Fig. 4). In case 1 and 2, WTC decreased significantly in all channel pairs. In case 4 and 5,

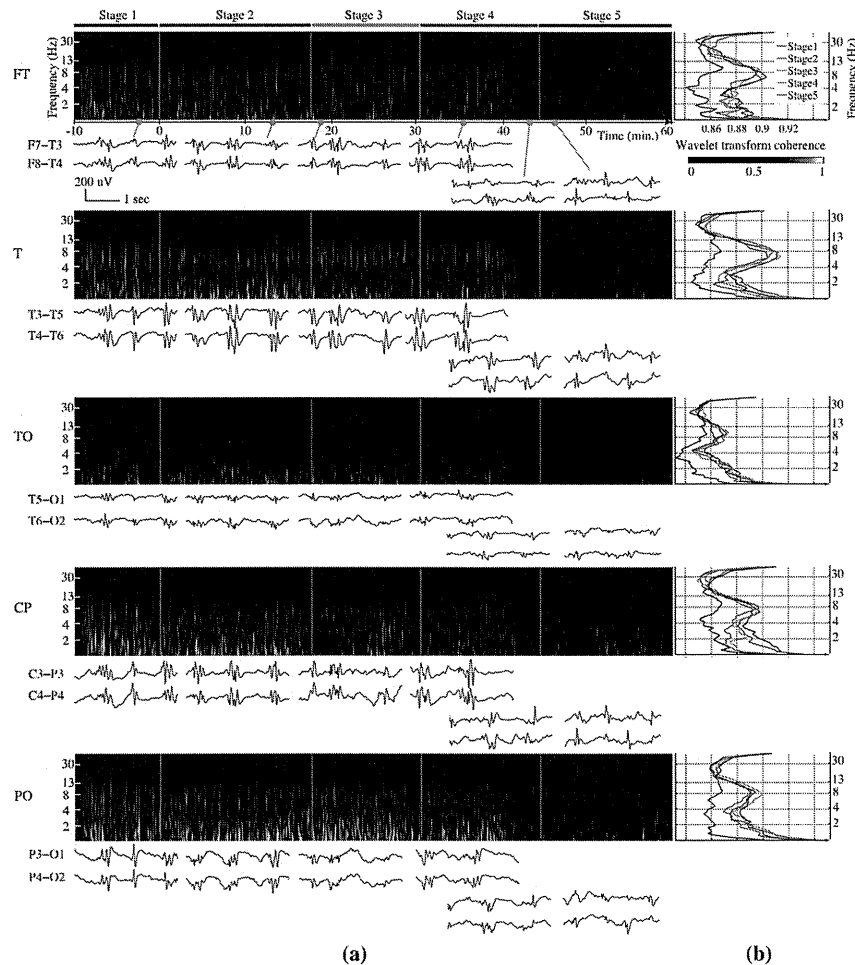(a)                                                                                      (b)

Fig. 3. Results of functional connectivity analysis in Case 1. (a) Spectra of wavelet transform coherence (WTC) and representative EEG waveforms. Colored areas of the spectra represent statistically significant WTCs estimated using a Monte Carlo method. The horizontal axis indicates relative time from the beginning of the anterior corpus callosotomy. Blue solid lines indicate the boundaries of corpus callosotomy stages. Typical waveforms corresponding to the time marked with gray circles on the time line are shown below each spectrum. For all channel combinations, the WTC during the posterior corpus callosotomy (Stage 4) decreased dramatically. (b) Averaged WTC of each stage. The dominant frequency range was 4–13 Hz. FT: F7–T3 and F8–T4, T: T3–T5 and T4–T6, TO: T5–O1 and T6–O2, CP: C3–P3 and C4–P4, PO: P3–O1 and P4–O2.

WTC decreased in all except the temporo-occipital channel pair. In case 3, the WTC of the temporal channel pair decreased with a small significance. The trend of WTC in case 6 didn't show significant changes.

3.3. Trend analysis

Fig. 5 shows the trend analysis of the range 4–13 Hz for all patients. Significant decreases in WTCs were observed during poster-

ior corpus callosotomy (Stage 4) in five patients (Cases 1–5) (Mann–Kendall test with FDR corrected $p < 0.05$ and Spearman's rank correlation coefficient $\rho > 0.5$). Three patients (Cases 1–3) showed decreasing trends only around the posterior part of corpus callosotomy (Stage 4), and two patients (Cases 4 and 5) showed decreasing trends starting from the anterior corpus callosotomy (Stage 2). No significant trends were seen in Case 6. As a sequence of callosal dissections performed, corresponding sequential changes in the synchronization of brain areas would be expected,
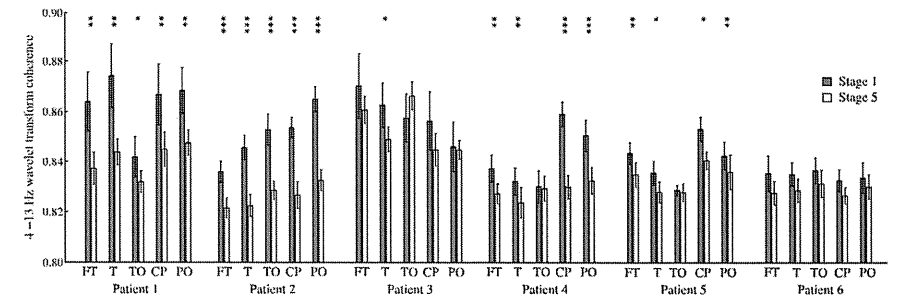
Fig. 4. Mean and standard deviation of stage-averaged wavelet transform coherence (WTC) before (Stage 1) and after (Stage 5) callosotomy ($^*p < 0.05$, $^{**}p < 0.01$, $^{***}p < 0.001$, FDR corrected, paired t-test). FT: F7–T3 and F8–T4, T: T3–T5 and T4–T6, TO: T5–O1 and T6–O2, CP: C3–P3 and C4–P4, PO: P3–O1 and P4–O2. The WTC of Cases 1 and 2 decreased after corpus callosotomy for all channel combinations. The WTC decreased in the other patients for some channel combinations, especially in channel pairs including temporal or parietal leads.

however, sequential decrease in WTC was not observed. In case 1, coherences of FT, T, CP, and PO decreased simultaneously during stage 4. Case 2 showed also simultaneous trend. In case 4, the coherence of CP and PO changed earlier than T.

Table 3 gives an overview of the results of trend analysis for all patients. The trend of Case 1 show a steeper Sen;s slope, that is, rapid decrease of connectivity. In contrast, the trend of Case 4 shows a gentler Sen's slope and slower decrease of connectivity over the long term through all callosotomy stages.

We additionally performed trend analyses on delta (1–4 Hz), theta (4–8 Hz), alpha (8–13 Hz), and beta (13–30 Hz) bands to investigate frequency-dependent changes of the inter-hemispheric coherence. The results were shown in Supplementary Fig. S1. The beta band did not present significant trend for all patients. The delta band showed similar trend with theta or alpha band in 4 patients. Thus, we assumed that the frequency-dependent changes were small in our study.

4. Discussion

This study demonstrated that time-varying inter-hemispheric connectivity during corpus callosotomy could be detected and quantified using the WTC and trend analysis techniques of intra-operative scalp EEG. Loss of bilateral coherence was not necessarily correlated with the stages of callosal sectioning, as bilateral coherence was less decreased during the early part of corpus callosotomy (Stage 2) but was markedly decreased after sectioning was completed (Stage 5) in 3 of 5 patients. This observation may support previous findings that total callosotomy is more likely to prevent drop attacks than partial callosotomy (Shimizu, 2005). The characteristics of the loss of coherence could be attributed to the inter-hemispheric connectivity of the background rhythms and the involvement of callosal connections in bilateral synchrony mechanisms. These findings show that intra-operative monitoring of bilateral EEG coherence is useful to estimate the physiological completeness of callosal sectioning.

4.1. Coherence analysis for quantification of inter-hemispheric connectivity

The present analytic approach has two advantages. First, the present procedure can detect 'non-stationary' changes in inter-hemispheric connectivity. Most conventional mathematical methods that examine periodicities in the frequency domain, such as

Fourier analysis, implicitly assume that the underlying processes are stationary in time. However, real electrophysiological recordings can only be approximated as quasi-stationary since the recording is stationary only within short intervals. Wavelet transforms expand time series into time frequency space and can therefore identify localized intermittent periodicities (Grinsted et al., 2004). Thus, WTC is particularly suited to quantifying time varying coherence (Sakkalis, 2011) and can be directly applied for 'online' quantification of the instantaneous coherence (Lachaux et al., 2002). Second, the present approach can provide 'objective quantification' including both spikes and background spontaneous activities. In general, EEG readers cannot easily identify changes in bilateral synchrony just by visual interpretation of raw waveforms, unless the bi-hemispheric epileptiform discharges are clearly dissociated. WTC provides a simple method to detect inter-hemispheric coherence, and trend analysis with the recursive algorithm can detect statistically significant short-term and long-term coherence changes.

4.2. EEG background connectivity and corpus callosum

Previous studies have suggested the importance of the corpus callosum in inter-hemispheric connectivity of EEG. The correlation between fiber density, measured with fractional anisotropy, and the peak frequency of occipital background alpha was strongest in the posterior corpus callosum (Valdés-Hernández et al., 2010). Diffusion tensor imaging showed that inter-hemispheric coherence of the temporo-parietal EEG in the alpha (8–12 Hz) band was significantly correlated with the integrity of posterior white matter tracts including the posterior corpus callosum (Teipel et al., 2009). Posterior inter-hemispheric EEG coherence (alpha and beta frequencies) was correlated significantly with the size of posterior corpus callosum area, and anterior coherence (delta, theta, and alpha frequencies) with the size of anterior corpus callosum area in Alzheimer patients (Pogarell et al., 2005).

Our study showed that 4–13 Hz (theta and alpha band) inter-hemispheric coherence decreased after corpus callosotomy, especially in the temporo-parietal and centro-parietal regions. This decrease in inter-hemispheric coherence frequently occurred during sectioning of the posterior corpus callosum. This finding is supported by previous studies on the importance of the posterior corpus callosum in the inter-hemispheric coherence of background rhythms. However, no region-specific changes in coherence were observed during particular stages of callosal sectioning, possibly
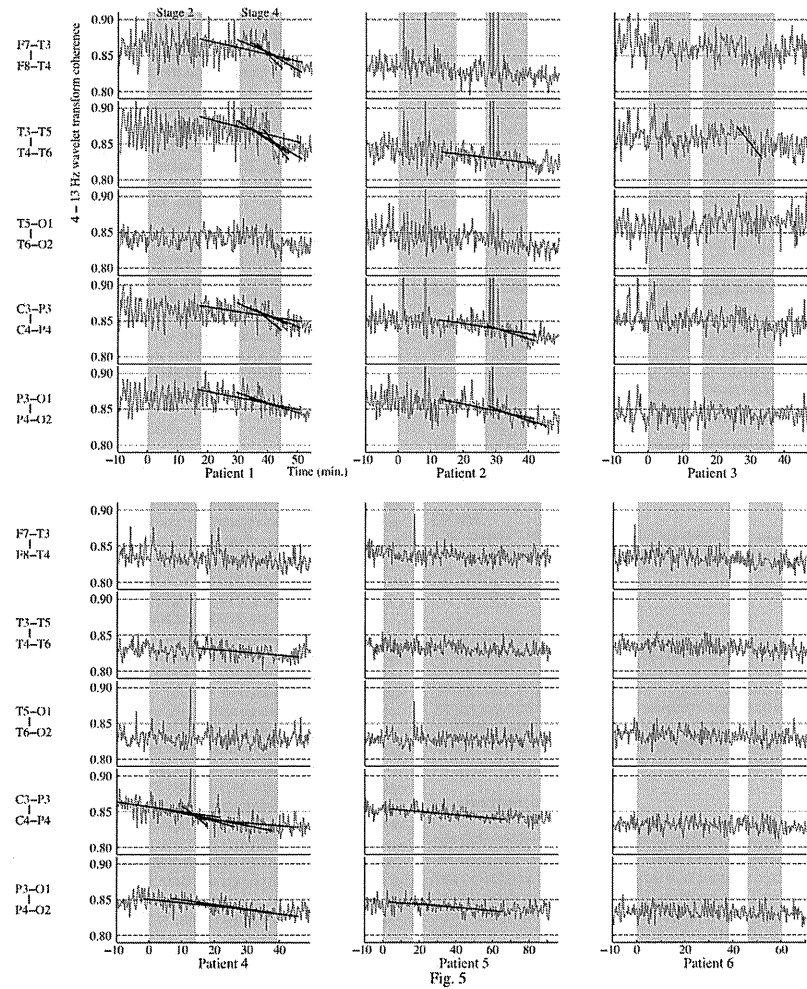
Fig. 5. Results of trend analysis averaged across the 4–13 Hz frequency range. Gray solid line indicates wavelet transform coherence (WTC) trend. Black solid lines indicate statistically significant Sen's slopes (Mann–Kendall test with FDR corrected $p < 0.05$ and Spearman's rank correlation coefficient $\rho > 0.5$). Cases 1–3 showed decreasing trends only during posterior corpus callosotomy (Stage 4; final-drop type), and Cases 4 and 5 showed decreasing trends starting during anterior corpus callosotomy (Stage 2; gradual-decrease type). No significant trends were seen in Case 6 (stable type).

due to frequency specificity in the brain regions. The present analysis was limited to 4–13 Hz activities, which were dominant in the power spectrogram. However, other frequency ranges may be more sensitive to detect changes in the inter-hemispheric coherence mediated by the anterior corpus callosum, or changes in the frontal area.

### 4.3. Bilateral synchrony of epileptiform discharges

The reduction of inter-hemispheric coherence may depend on the relative contribution of the thalamo-cortical network to callosal interaction in the genesis of bilateral synchrony. Two types of network may be involved in the generation of bilateral synchrony;

**Table 3**
Summary of WTC trend analysis across the 4–13 Hz frequency range.

| Case No. | Channel pair | Trend statistics | | Correlation | Duration of trend (min) | Stages | | | | |
|---|---|---|---|---|---|---|---|---|---|---|
| | | $Z_{MK}$ | Sen's slope | | | 1 | 2 | 3 | 4 | 5 |
| 1 | F7–T3: F8–T4 | −5.874** | −0.0024 | −0.744 | 17.2 | | | | + | + |
| | | −4.407** | −0.0009 | −0.576 | 34.3 | | + | + | + | + |
| | | −4.394** | −0.0017 | −0.615 | 17.2 | | | + | + | + |
| | | −3.989** | −0.0041 | −0.555 | 8.6 | | | | + | + |
| | T3–T5: T4–T6 | −4.764** | −0.0025 | −0.616 | 17.2 | | | | + | + |
| | | −4.630** | −0.0011 | −0.614 | 33.8 | | + | + | + | + |
| | | −4.509** | −0.0027 | −0.594 | 17.2 | | | + | + | + |
| | | −4.151** | −0.0049 | −0.525 | 8.7 | | | | + | + |
| | T4–O1: T6–O2 | n/s | | | | | | | | |
| | C3–P3: C4–P4 | −4.190** | −0.0017 | −0.568 | 17.2 | | | | + | + |
| | | −4.133** | −0.0018 | −0.556 | 16.9 | | | + | + | + |
| | | −4.075** | −0.0007 | −0.554 | 34.4 | | + | + | + | + |
| | | −3.850* | −0.0036 | −0.515 | 8.4 | | | | + | + |
| | P3–O1: P4–O2 | −6.104** | −0.0008 | −0.737 | 34.4 | | + | + | + | + |
| | | −4.509** | −0.0012 | −0.575 | 17.2 | | | + | + | + |
| | | −4.028** | −0.0014 | −0.504 | 16.9 | | | | + | + |
| 2 | F7–T3: F8 – T4 | n/s | | | | | | | | |
| | T3–T5: T4–T6 | −4.303** | −0.0006 | −0.570 | 28.7 | | + | + | + | + |
| | T4–O1: T6–O2 | n/s | | | | | | | | |
| | C3–P3: C4–P4 | −4.698** | −0.0007 | −0.619 | 29.7 | | + | + | + | + |
| | | −4.076* | −0.0015 | −0.508 | 14.9 | | | | + | + |
| | P3–O1: P4–O2 | −5.742** | −0.0009 | −0.703 | 28.7 | | + | + | + | + |
| | | −4.956** | −0.0017 | −0.621 | 14.6 | | | | + | + |
| | | −4.905** | −0.0015 | −0.612 | 14.6 | | | | + | + |
| 3 | F7–T3: F8–T4 | n/s | | | | | | | | |
| | T3–T5: T4–T6 | −4.509** | −0.0060 | −0.563 | 7.4 | | | | + | |
| | T4–O1: T6–O2 | n/s | | | | | | | | |
| | C3–P3: C4–P4 | n/s | | | | | | | | |
| | P3–O1: P4–O2 | n/s | | | | | | | | |
| 4 | F7–T3: F8–T4 | n/s | | | | | | | | |
| | T3–T5: T4–T6 | −4.303** | −0.0004 | −0.540 | 31.0 | | | + | + | + |
| | T4–O1: T6–O2 | n/s | | | | | | | | |
| | C3–P3: C4–P4 | −5.833** | −0.0009 | −0.719 | 31.1 | | + | + | + | |
| | | −5.466** | −0.0009 | −0.687 | 31.6 | + | + | + | + | |
| | | −4.560** | −0.0007 | −0.586 | 31.5 | + | + | + | + | |
| | | −4.447** | −0.0036 | −0.582 | 7.7 | | | + | + | |
| | | −3.939* | −0.0013 | −0.504 | 16.0 | | | + | + | |
| | | −3.924* | −0.0004 | −0.507 | 31.0 | | | + | + | + |
| | P3–O1: P4–O2 | −6.317** | −0.0007 | −0.755 | 31.1 | | + | + | + | |
| | | −5.491** | −0.0006 | −0.658 | 31.6 | | + | + | + | + |
| | | −4.943** | −0.0005 | −0.605 | 31.6 | + | + | + | + | |
| 5 | F7–T3: F8–T4 | n/s | | | | | | | | |
| | T3–T5: T4–T6 | n/s | | | | | | | | |
| | T4–O1: T6–O2 | n/s | | | | | | | | |
| | C3–P3: C4–P4 | −4.407* | −0.0002 | −0.569 | 50.1 | | | + | + | + |
| | | −4.369* | −0.0002 | −0.529 | 50.3 | | | + | + | |
| | P3–O1: P4–O2 | −4.382* | −0.0002 | −0.555 | 50.1 | | | + | + | + |
| | | −4.088* | −0.0002 | −0.511 | 50.9 | | | + | + | + |
| 6 | F7–T3: F8–T4 | n/s | | | | | | | | |
| | T3–T5: T4–T6 | n/s | | | | | | | | |
| | T4–O1: T6–O2 | n/s | | | | | | | | |
| | C3–P3: C4–P4 | n/s | | | | | | | | |
| | P3–O1: P4–O2 | n/s | | | | | | | | |

n/s: no significance, +: stages overlapping significant trend.
* $p < 0.05$.
** $p < 0.01$ (FDR corrected, Mann–Kendall Z-score).

the thalamo-cortical network, and the cortico-cortical (callosal) network. The classical centrencephalic hypothesis has long been proposed for the generation of generalized epileptiform discharges (Jasper and Kershman, 1941; Penfield and Erickson, 1941). Physiological investigations have proven that the thalamo-cortical system is important in the genesis of generalized EEG patterns including sleep and bilaterally synchronous epileptiforms (Steriade et al., 1993). Although the thalamo-cortical network is key for the maintenance of generalized spike wave discharges, cortical neurons are currently believed to be the actual generator or "trigger" of these activities (Timofeev and Steriade, 2004). In a cat model of generalized spike wave seizures, 2–3 Hz spike waves spread

from one cortical area to another well before reaching the thalamus. After the cortico-cortical connection between two cortical areas is cut, a minority of thalamo-cortical neurons can still fire spike-bursts during cortically generated spike wave seizures, thus partially recovering the synchronization between two separated cortical areas (Neckelmann et al., 1998).

As the sequence of dissection was always anterior to posterior in the present study, it is difficult to conclude that the posterior part of the corpus callosum plays a particular role for the degree of coherence measured, or that completeness per se is relevant for desynchronization of EEG. Palm et al. (2011) reported that electroencephalographic recordings during electroconvulsive therapy

(ECT) showed a complete inter-hemispheric synchronicity in a patient with agenesis of the corpus callosum. This indicates that the inter-hemispheric synchronicity can be established without major commissural connections between neocortices.

The present study identified three different types of time-varying inter-hemispheric coherence. In the final-drop type, the bilateral coherence decreases in the final stage of corpus callosotomy (Cases 1–3); in the gradual-decrease type, bilateral coherence decreases gradually during all stages of corpus callosotomy (Cases 4 and 5); and in the stable type, no significant change occurs (Case 6). Based on the pathways described above, the final-drop type might be considered to involve a relatively dominant cortico-cortical pathway with asymmetric distribution of the anatomical pathways of the electrophysiological inter-hemispheric connectivity around the posterior part of the corpus callosum. The gradual-decrease type might be considered to involve a relatively dominant cortico-cortical pathway with even distribution of the anatomical pathways of the electrophysiological inter-hemispheric connectivity throughout the corpus callosum. The stable type might be considered to involve a relatively dominant cortico-subcortical pathway or largely lateralized electrophysiological activities before corpus callosotomy. Thus our analysis of intra-operative inter-hemispheric coherence may reveal the transition from the state in which both cortico-cortical and cortico-subcortical pathways exist, to the state in which the cortico-subcortical pathway is dominant. Whether such intra-operative acute changes under anesthesia represent extra-operative chronic outcome in EEG requires verification. In this small case series, the loss of coherence and its pattern were not clearly associated with the post-operative EEG findings and seizure outcome. Further case experience is necessary to reveal the clinical implications of our method.

This study has certain limitations regarding the observed frequency of spikes. The amount of epileptic activities contained in the analysis depended on the frequency of spikes. Analysis targeting the spikes may be preferable, but actually, for patients with low frequency spikes (Cases 2, 4, and 5 in Table 2), the spike-extraction approach was difficult to perform. Consequently, this study observed no clear correlation between the frequency of spikes and coherence trend.

### 4.4. Application to epilepsy surgery

The final-drop type of our study may indicate that corpus callosotomy is not fully effective unless entire corpus callosum is sectioned. The superior efficacy of complete over partial callosotomy is well known. Few patients (0–10%) become completely seizure free after callosotomy, although some seizure types, especially tonic and atonic seizures, may be completely abolished (Maehara and Shimizu, 2001; Hanson et al., 2002; Wong et al., 2006; Cukiert et al., 2006). Complete arrest of drop attacks (atonic and tonic seizures) may be observed in up to 91% of pediatric patients after total callosotomy, but in only 67% after partial callosotomy (Shimizu, 2005). Furthermore, relatively high rates of complete seizure remission were achieved after total corpus callosotomy in a subgroup of patients with intractable epilepsy following West syndrome or Lennox-Gastaut syndrome (Iwasaki et al., 2012). On the other hand, anterior callosotomy with sparing of splenium can preserve sufficient fibers for inter-hemispheric transfer of some perceptual information and diminish the complications of disconnection syndrome (Funnell et al., 2000; Wong et al., 2006; Jenssen et al., 2006; Turanli et al., 2006).

Fiol et al. reported that the degree of lateralization of generalized epileptiform discharges (GED) did not correlate with degree of reduction of tonic-atonic seizures, and that intraoperative surface EEG monitoring does not appear to be helpful as a guide to extent of callosotomy, although lateralization of GED after corpus

callosum sectioning was evident in 78% of patients with GED. Our results correspond with their study in terms of correlation with seizure outcome. The number of patients included in our study is quite low, thus more patients must be investigated to evaluate the relationship between the present findings and seizure outcome. To reveal the relationship between the electrophysiological phenomena and the seizure outcome, we consider that further approach from the viewpoint of sub-cortical and hierarchical network is necessary.

## 5. Conclusion

The present study showed that loss of inter-hemispheric coherence is not always correlated with the stages of callosal sectioning. Inter-hemispheric coherence decreases at the final stage of corpus callosotomy, so the effect of corpus callosotomy is only maximized after complete sectioning. The present method of evaluating time-varying inter-hemispheric EEG coherence may be useful to monitor the physiological completeness of corpus callosotomy.

## Acknowledgements

## Appendix A. Supplementary data

Supplementary data associated with this article can be found, in the online version, at http://dx.doi.org/10.1016/j.clinph.2013.05.004.

## References

Asadi-Pooya AA, Sharan A, Nei M, Sperling MR. Corpus callosotomy. Epilepsy Behav 2008;13:271–8.
Chang C, Glover G. Time frequency dynamics of resting-state brain connectivity measured with fMRI. Neuroimage 2010;50:81–98.
Clarke DF, Wheless JW, Chacon MM, Breier J, Koenig MK, McManis M, et al. Corpus callosotomy: a palliative therapeutic technique may help identify respectable epileptogenic foci. Seizure 2007;16:545–53.
Cukiert A, Burattini JA, Mariani PP, Câmara RB, Seda L, Baldauf CM, et al. Extended, one-stage callosal section for treatment of refractory secondarily generalized epilepsy in patients with Lennox-Gastaut and Lennox-like syndromes. Epilepsia 2006;47:371–4.
Fiol ME, Gates JR, Mireles R, Maxwell RE, Erickson DM. Value of intraoperative EEG changes during corpus callosotomy in predicting surgical results. Epilepsia 1993;34:74–8.
Funnell MG, Corballis PM, Gazzaniga MS. Cortical and subcortical interhemispheric interactions following partial and complete callosotomy. Arch Neurol 2000;57:185–9.
Genovese CR, Lazar NA, Nichols T. Thresholding of statistical maps in functional neuroimaging using the false discovery rate. Neuroimage 2002;15:870–8.
Grinsted A, Moore JC, Jevrejeva S. Application of the cross wavelet transform and wavelet coherence to geophysical time series. Nonlinear Process Geophys 2004;11:561–6.
Hanson RR, Risinger M, Maxwell R. The ictal EEG as a predictive factor for outcome following corpus callosum section in adults. Epilepsy Res 2002;49:89–97.
Iwasaki M, Nakasato N, Kakisaka Y, Kanno A, Uematsu M, Haginoya K, et al. Lateralization of interictal spikes after corpus callosotomy. Clin Neurophysiol 2011;122:2121–7.
Iwasaki M, Uematsu M, Sato Y, Nakayama T, Haginoya K, Osawa S, et al. Complete remission of seizures after corpus callosotomy. J Neurosurg Pediatr 2012;10:7–13.
Jaagus J. Climatic changes in Estonia during the second half of the 20th century in relationship with changes in large-scale atmospheric circulation. Theor Appl Climatol 2006;83:77–88.
Jasper HH, Kershman J. Electroencephalographic classification of the epilepsies. Arch Neurol Psychiatry 1941;45:903–43.

Jenssen S, Sperling MR, Tracy JI, Nei M, Joyce L, David G, et al. Corpus callosotomy in refractory idiopathic generalized epilepsy. Seizure 2006;15:621–9.
Kaas JH. The organization of callosal connections in primates. In: Reeves AG, Roberts DW, editors. Epilepsy and the corpus callosum 2. Advances in behavioral biology, vol. 45. New York: Plenum Press; 1995. p. 15–27.
Kendall MG. A new measure of rank correlation. Biometrika 1938;30:81–93.
Knyazeva MG, Innocenti GM. EEG coherence studies in the normal brain and after early-onset cortical pathologies. Brain Res Brain Res Rev 2001;36(2–3):119–28.
Lachaux JP, Lutz A, Rudrauf D, Le Van Quyen M, Martinerie J, et al. Estimating the time-course of coherence between single-trial brain signals: an introduction to wavelet coherence. Neurophysiol Clin 2002;32:157–74.
Lemieux JF, Blume WT. Topographical evolution of spike–wave complexes. Brain Res 1986;373:275–87.
Lin JH, Kwan SY. Post-section recruitment of epileptiform discharges in electrocorticography during callosotomy in 48 patients with Lennox-Gastaut syndrome. J Clin Neurosci 2012;19:388–93.
Maehara T, Shimizu H. Surgical outcome of corpus callosotomy in patients with drop attacks. Epilepsia 2001;42:67–71.
Mallat S. A wavelet tour of signal processing. London, UK: Academic Press; 1999. pp. 79–88.
Matsuo A, Ono T, Baba H, Ono K. Callosal role in generation of epileptiform discharges: quantitative analysis of EEGs recorded in patients undergoing corpus callosotomy. Clin Neurophysiol 2003;114:2165–71.
Matsuzaka T, Ono K, Baba H, Matsuo M, Tanaka S, Kamimura N, et al. Quantitative EEG analyses and surgical outcome after corpus callosotomy. Epilepsia 1999;40:1269–28.
Montplaisir J, Nielsen T, Côté J, Boivin D, Rouleau I, Lapierre G. Interhemispheric EEG coherence before and after partial callosotomy. Clin Electroencephalogr 1990;21(1):42–7.
Muller K, Lohmann G, Neumann J, Grigutsch M, Mildner T, von Cramon DY. Investigating the wavelet coherence phase of the BOLD signal. J Magn Reson Imaging 2004;20:145–52.
Musiek FE. Neuroanatomy, neurophysiology, and central auditory assessment: Part III. Corpus callosum and efferent pathways. Ear Hear 1986;7:349–58.
Neckelmann D, Amzica F, Steriade M. Spike–wave complexes and fast components of cortically generated seizures. III. Synchronizing mechanisms. J Neurophysiol 1998;80:1480–94.
Nolte G, Bai O, Wheaton L, Mari Z, Vorbach S, Hallett M. Identifying true brain interaction from EEG data using the imaginary part of coherency. Clin Neurophysiol 2004;115:2292–307.
Oguni H, Andermann F, Gotman J, Olivier A. Effect of anterior callosotomy on bilaterally synchronous spike and wave and other EEG discharges. Epilepsia 1994;35:505–13.
Palm U, Forsthoff A, de la Fontaine L, Rupprecht T, Karch S, Meisenzahl EM, et al. Electroconvulsive therapy and corpus callosum aplasia: a case report. J ECT 2011;27(1):e17–20.
Penfield W, Erickson TC. Epilepsy and cerebral localization, Springfield, IL: Charles Thomas; 1941.
Pinkofsky HB, Struve FA, Meyer MA, Patrick G, Reeves RR. Decreased multi-band posterior interhemispheric coherence with a lipoma on the corpus callosum: a case report of a possible association. Clin Electroencephalogr 1997;28(3):155–9.
Pogarell O, Teipel SJ, Juckel G, Gootjes L, Möller T, Bürger K, et al. EEG coherence reflects regional corpus callosum area in Alzheimer's disease. J Neurol Neurosurg Psychiatry 2005;76:109–11.
Quattrini A, Papo I, Cesarano R, Fioravanti P, Paggi A, Ortenzi A, et al. EEG patterns after callosotomy. J Neurosurg Sci 1997;41:85–92.
Sakkalis V. Review of advanced techniques for the estimation of brain connectivity measured with EEG/MEG. Comput Biol Med 2011;41:1110–7.
Sen PK. Estimates of the regression coefficient based on Kendall's tau. J Am Stat Assoc 1968;63:1379–89.
Shimizu H. Our experience with pediatric epilepsy surgery focusing on corpus callosotomy and hemispherectomy. Epilepsia 2005;46(Suppl 1):30–1.
Spencer SS, Katz A, Ebersole J, Novotny E, Mattson R. Ictal EEG changes with corpus callosum section. Epilepsia 1993;34:568–73.
Steriade M, McCormick DA, Sejnowski TJ. Thalamocortical oscillations in the sleeping and aroused brain. Science 1993;262:679–85.
Teipel SJ, Pogarell O, Meindl T, Dietrich O, Sydykova D, Hunklinger U, et al. Regional networks underlying interhemispheric connectivity: an EEG and DTI study in healthy ageing and amnestic mild cognitive impairment. Hum Brain Mapp 2009;30:2098–119.
Thatcher RW, Krause PJ, Hrybyk M. Cortico-cortical associations and EEG coherence: a two-compartmental model. Electroencephalogr Clin Neurophysiol 1986;64(2):123–43.
Timofeev I, Steriade M. Neocortical seizures: initiation, development and cessation. Neuroscience 2004;123:299–336.
Torrence C, Compo G. A practical guide to wavelet analysis. Bull Am Meteorol Soc 1998;79:61–78.
Torrence C, Webster P. Interdecadal changes in the ENSO-Monsoon system. J Clim 1999;12:2679–90.
Turanli G, Yalnizoglu D, Genc-Acikgoz D, Akalan N, Topcu M. Outcome and long term follow-up after corpus callosotomy in childhood onset intractable epilepsy. Childs Nerv Syst 2006;22:1322–7.
Valdés-Hernández PA, Ojeda-González A, Martínez-Montes E, Lage-Castellanos A, Virués-Alba T, Valdés-Urrutia L, et al. White matter architecture rather than cortical surface area correlates with the EEG alpha rhythm. Neuroimage 2010;49:2328–39.
Wada JA. Midline subcortical structures for transhemispheric ictal and interictal transmission. In: Reeves AG, Roberts DW, editors. Epilepsy and the corpus callosum 2. Advances in behavioral biology, vol. 45. New York: Plenum; 1995. p. 61–78.
Waxman SG. Lange clinical neuroanatomy, 25th ed. New York: McGraw-Hill; 2003.
Wong TT, Kwan SY, Chang KP, Hsiu-Mei W, Yang TF, Chen YS, et al. Corpus callosotomy in children. Childs Nerv Syst 2006;22:999–1011.

Hindawi

*Research Article*

# Effectiveness of Variable-Gain Kalman Filter Based on Angle Error Calculated from Acceleration Signals in Lower Limb Angle Measurement with Inertial Sensors

### Yuta Teruyama and Takashi Watanabe

*Graduate School of Biomedical Engineering, Tohoku University, Sendai 980-8579, Japan*

Correspondence should be addressed to Yuta Teruyama; yuta.teruyama@bme.tohoku.ac.jp

The wearable sensor system developed by our group, which measured lower limb angles using Kalman-filtering-based method, was suggested to be useful in evaluation of gait function for rehabilitation support. However, it was expected to reduce variations of measurement errors. In this paper, a variable-Kalman-gain method based on angle error that was calculated from acceleration signals was proposed to improve measurement accuracy. The proposed method was tested comparing to fixed-gain Kalman filter and a variable-Kalman-gain method that was based on acceleration magnitude used in previous studies. First, in angle measurement in treadmill walking, the proposed method measured lower limb angles with the highest measurement accuracy and improved significantly foot inclination angle measurement, while it improved slightly shank and thigh inclination angles. The variable-gain method based on acceleration magnitude was not effective for our Kalman filter system. Then, in angle measurement of a rigid body model, it was shown that the proposed method had measurement accuracy similar to or higher than results seen in other studies that used markers of camera-based motion measurement system fixing on a rigid plate together with a sensor or on the sensor directly. The proposed method was found to be effective in angle measurement with inertial sensors.

## 1. Introduction

Wearable inertial sensors have been used in many studies to estimate human kinetic data. Those sensors have advantages of low cost, small size, and practical usefulness compared to traditional lab tools such as optical motion measurement system or electric goniometers. As has been reported in previous studies, segment and joint angles [1–11], stride length [1, 3, 5], walking speed [1, 5], gait event timing [5, 12, 13], and so on can be estimated using inertial sensors. Therefore, a wearable inertial sensor system can be effective for objective and quantitative evaluation in rehabilitation of motor function. That is, inertial sensors are considered to be suitable for clinical applications.

In our previous studies, a method of measuring lower limb angles using wireless inertial sensors was developed to realize simplified wearable gait evaluation system for rehabilitation support. The method was tested in measurement of gait of healthy subjects [14, 15]. Although the method was shown to have practical accuracy, measurement errors varied depending on movement speeds or subjects. In the angle measurement method of our previous studies, Kalman filter was applied using angle calculated from acceleration signals. Many other studies also used accelerometers as inclinometers to measure inclination angles of body segments [2, 5, 7, 8]. However, the angle calculated from acceleration signals was influenced by impact and movement accelerations, since the angle was calculated from gravitational acceleration. Therefore, those impact and movement accelerations can be considered as one of the causes of variation of measurement error.

Low-pass filtering of acceleration signals is one of the methods to reduce influences of those impact and motion accelerations. In our previous studies, outputs of accelerometer were filtered with Butterworth low-pass filter with cutoff frequency of 0.5 Hz [14, 15]. However, low cutoff frequency is at risk for increasing measurement error because of its large time constant in the low-pass filtering. Therefore,

using higher cutoff frequency has a possibility to improve measurement error.

In this paper, in order to reduce influences of impact and movement accelerations in calculation of angles using Kalman filter, a variable-Kalman-gain method with higher cutoff frequency for the low-pass filtering was tested. In previous studies, a method to change Kalman gain based on the magnitude of acceleration signals was used [9, 16]. However, in this study, the method to change Kalman gain based on error of angle calculated from acceleration signals was proposed. This is because the Kalman filter of our system is applied using the angles calculated from acceleration signals.

The variable-gain method was evaluated in measurement of lower limb angles of healthy subjects in treadmill walking using a camera-based motion measurement system to measure reference angles for evaluation. The fixed-Kalman-gain method and the variable-gain method based on magnitude of acceleration signals were compared to the proposed method. Then, similar evaluation was performed in measurement of angles of a rigid body model, because some other studies evaluated angle measurement method with inertial sensors using a rigid plate that fixed a sensor together with markers of an optical motion measurement system or attaching the markers directly on the sensor [4, 8, 10, 11].

## 2. Angle Measurement Method Based on Kalman Filter

### 2.1. Fixed-Kalman-Gain Method.
Figure 1(a) shows the block diagram of the angle measurement method used in our previous studies. An inclination angle of body segment is calculated by integrating an output of a gyroscope. Here, the integration error is corrected by Kalman filter using the angle calculated from outputs of an accelerometer. Then, joint angle is calculated from difference of inclination angles of the adjacent segments.

The state equation is represented by error of angle measured with a gyroscope $\Delta\theta$ and bias offset of outputs of the gyroscope $\Delta b$ as follows:

$$\begin{bmatrix} \Delta\theta_{k+1} \\ \Delta b_{k+1} \end{bmatrix} = \begin{bmatrix} 1 & \Delta t \\ 0 & 1 \end{bmatrix} \begin{bmatrix} \Delta\theta_k \\ \Delta b_k \end{bmatrix} + \begin{bmatrix} \Delta t \\ 1 \end{bmatrix} w, \tag{1}$$

where $w$ is error in measurement with the gyroscope and $\Delta t$ is sampling period. Observation signal is deference of angles obtained from the gyroscope and an accelerometer $\Delta y$, which is given by

$$\Delta y_k = \begin{bmatrix} 1 & 0 \end{bmatrix} \begin{bmatrix} \Delta\theta_k \\ \Delta b_k \end{bmatrix} + v, \tag{2}$$

where $v$ is error in measurement with the accelerometer. On this state-space model, Kalman filter repeats corrections (3) and predictions (4):

$$\begin{bmatrix} \Delta\hat{\theta}_k \\ \Delta\hat{b}_k \end{bmatrix} = \begin{bmatrix} \Delta\hat{\theta}_k^- \\ \Delta\hat{b}_k^- \end{bmatrix} + \begin{bmatrix} K_1 \\ K_2 \end{bmatrix} \left( \Delta y_k - \Delta\hat{\theta}_k^- \right), \tag{3}$$

$$\begin{bmatrix} \Delta\hat{\theta}_{k+1}^- \\ \Delta\hat{b}_{k+1}^- \end{bmatrix} = \begin{bmatrix} 1 & \Delta t \\ 0 & 1 \end{bmatrix} \begin{bmatrix} \Delta\hat{\theta}_k \\ \Delta\hat{b}_k \end{bmatrix}, \tag{4}$$

where $K_1$ and $K_2$ represent Kalman gain for $\Delta\theta$ and $\Delta b$, respectively. Notations such as $\Delta\hat{\theta}$ and $\Delta\hat{\theta}^-$ represent estimated value and predicted value for $\Delta\theta$, respectively. For the initial condition, $\Delta\hat{\theta}_0^-$ was set as 0, and $\Delta\hat{b}_0^-$ was set as $\Delta b$ at the last measurement. The Kalman filter was applied repeatedly until its output converged.

Values of Kalman gain were fixed in angle calculation in our previous studies. Those gain values are determined by the noise ratio, that is, the ratio of the covariance of observation noise and covariance of process noise. In our system, value of Kalman gain increases as the noise ratio decreases and decreases as the noise ratio increases.

As shown in (3) and (4), the Kalman filter estimates $\Delta\theta$ and $\Delta b$ by using the angle difference $\Delta y$. Therefore, large value of Kalman gain (small noise ratio) means that calculation results become highly dependent on accelerometer, while small Kalman gain (large noise ratio) means that calculation results become highly dependent on gyroscope. Considering power of the correction by Kalman filter, values of the noise ratio were determined by trial and error method.

### 2.2. Variable-Kalman-Gain Method.
The fixed-Kalman-gain method shown in the previous section was found to be useful in measurement of angles during gait of healthy subjects [14, 15]. However, impact and movement accelerations were considered to increase measurement error and its variation. That is, those accelerations are considered to cause inappropriate correction by the Kalman filter. As described in the previous section, Kalman gain means correction power of the Kalman filter. Therefore, in this paper, following two methods of changing the noise ratio to determine Kalman gain were tested.

(a) *Acceleration Magnitude-Based Method.* Figure 1(b) shows the variable-gain method based on acceleration magnitude, which was introduced in reference to previous studies [9, 16]. Value of the noise ratio is adjusted based on the magnitude of impact and motion acceleration signals. Here, the magnitude of impact and motion acceleration signals was calculated by subtracting gravitational acceleration (1 G) from magnitude of measured acceleration vector. That is, the value of noise ratio is varied as follows:

$$\begin{aligned} n = n_1, & \quad \text{for } |\alpha| \le \alpha_1, \\ n = n_2, & \quad \text{for } \alpha_1 < |\alpha| \le \alpha_2, \\ n = n_3, & \quad \text{for } \alpha_2 < |\alpha| \le \alpha_3, \\ n = n_4, & \quad \text{for } \alpha_3 < |\alpha|, \end{aligned} \tag{5}$$

where $n$ and $|\alpha|$ represent the noise ratio and the magnitude of impact and motion acceleration signals, respectively. $\alpha_1$, $\alpha_2$, and $\alpha_3$ show thresholds to change the value of noise ratio, respectively.

(b) *Angle Error-Based Method.* Figure 1(c) shows the method proposed in this paper, in which the noise ratio is adjusted based on the difference between the angle estimated by the Kalman filter and the angle calculated from acceleration signals. Here, the angle difference was used approximately as the

(a) Fixed Kalman gain method

(b) Variable-Kalman-gain method based on acceleration magnitude

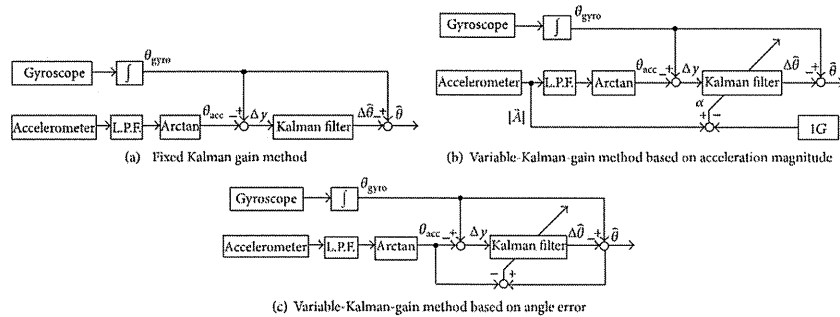(c) Variable-Kalman-gain method based on angle error

FIGURE 1: Block diagrams of the angle calculation methods using Kalman filter tested in this paper.

magnitude of influence of impact and motion accelerations. That is, it was assumed that the angle difference involves substantial error of angle calculated from acceleration signals, which is caused by impact and movement accelerations. The value of noise ratio is varied as follows:

$$n = n_1, \quad \text{for } |\hat{\theta} - \theta_{acc}| \leq \theta_1,$$
$$n = n_2, \quad \text{for } \theta_1 < |\hat{\theta} - \theta_{acc}| \leq \theta_2,$$
$$n = n_3, \quad \text{for } \theta_2 < |\hat{\theta} - \theta_{acc}| \leq \theta_3, \quad (6)$$
$$n = n_4, \quad \text{for } \theta_3 < |\hat{\theta} - \theta_{acc}|,$$

where, $n$ and $|\hat{\theta} - \theta_{acc}|$ represent the noise ratio and the angle difference between the angle estimated by the Kalman filter $\hat{\theta}$ and the angle calculated from acceleration signals $\theta_{acc}$, respectively. The angle difference $|\hat{\theta} - \theta_{acc}|$ shows approximately the magnitude of influence of impact and motion accelerations. $\theta_1$, $\theta_2$, and $\theta_3$ show thresholds to change values of the noise ratio, respectively.

## 3. Methods of Validation Tests

The angle calculation methods were applied to data measured with inertial sensors and evaluated in comparison to those angles measured with an optical motion measurement system. First, the evaluation was performed in measurement of lower limb angles in treadmill walking with healthy subjects. Then, angles of a rigid body model were measured for evaluation of the methods, because some other studies evaluated their angle measurement method with inertial sensors using the rigid plate that fixed a sensor together with markers of an optical motion measurement system [4, 8, 10, 11].

*3.1. Measurement of Lower Limb Angles in Treadmill Walking.* Inclination angles of lower limb segments in treadmill walking were measured with 3 healthy subjects (male, 22-23 y.o.). The subjects walked on a treadmill for about 90 sec at

speeds of 1 km/h (slow), 3 km/h (normal), and 5 km/h (fast). Five trials were performed for each walking speed.

Seven wireless inertial sensors (WAA-006, Wireless Technologies) were attached on the feet, the shanks and the thighs of both legs, and lumbar region with stretchable bands (Figure 2(a)). The sensors were put inside of pocket of the band. Acceleration and angular velocity signals of each sensor were measured with a sampling frequency of 100 Hz and were transmitted to a PC via Bluetooth network.

The optical motion measurement system (Optotrak, Northern Digital, Inc.) was used to measure reference data for evaluating angles calculated by the methods from data measured with the inertial sensors. Markers for reference data were attached on the left side of the body (Figure 2(a)). The maker positions were measured with a sampling frequency of 100 Hz.

*3.2. Measurement of Angles with a Rigid Body Model.* Figure 2(b) shows the schematic diagram of the rigid body model used in the measurement. The rigid body model simulated motion of the thigh, the shank, and the knee joint. The optical motion measurement system (Optotrak, Northern Digital, Inc.) was also used to measure reference data for evaluating the angle calculation method. Sensors and markers were attached on the rigid body model as shown in Figure 2(b). Acceleration and angular velocity signals of each sensor and the marker positions were measured with sampling frequency of 100 Hz.

Inclination angles of the thigh and the shank parts were measured for 35 sec with angle ranges of ±15, ±30, ±45, ±60, and ±75 deg for the thigh part. Zero degree means the direction of gravitational force. The shank part was moved freely associated with movement of the thigh part. The cycle period of the movements was 2 sec, and five trials were conducted for each target angle range.

## 4. Results of Validation Tests

Two variable-Kalman-gain methods were evaluated in comparison to the previous fixed-Kalman-gain method. Here, for

Sensor
● Optotrak marker

(a)
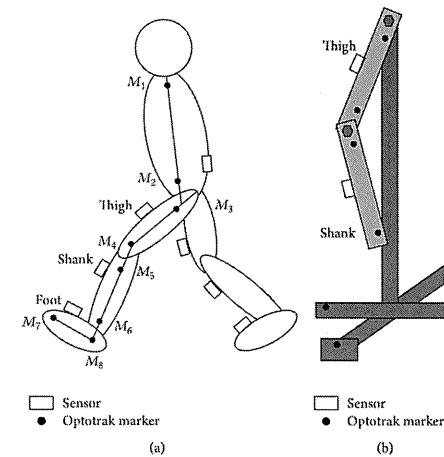
Sensor
● Optotrak marker

(b)

FIGURE 2: Experimental setup for the angle measurement during treadmill walking (a) and the angle measurement using rigid body model (b). M1: the acromion, M2: along the long axis of the trunk at the same height as the iliospinale anterius, M3: the great trochanter, M4: the lateral femoral condyle, M5: the caput fibulae, M6: the lateral malleolus, M7: the metatarsale fibulare, and M8: on the foot at the same height as the metatarsale fibulare along the line of shank markers.

the fixed-gain method, values of the noise ratio $n$ to determine Kalman gain and the cutoff frequency of Butterworth low-pass filter for acceleration signals $f_c$ are shown below.

Method 1 (previous fixed Kalman gain method)

$$n = 10^6, \qquad f_c = 0.5 \text{ Hz}. \qquad (7)$$

Method 2 (fixed Kalman gain method)

$$n = 10^6, \qquad f_c = 10 \text{ Hz}. \qquad (8)$$

Method 1 is the previous method used in our research group, in which the noise ratio of Kalman filter was fixed and cutoff frequency of the low-pass filter for acceleration signals was determined to remove impact and motion accelerations. Method 2 is the fixed-Kalman-gain method with higher cutoff frequency of the low-pass filter, which was tested to make clear the influence of low cutoff frequency on measurement error.

There was offset difference between the sensor system and camera-based motion analysis system, because the markers for the reference signals were not attached on the sensors. Therefore, the difference was calculated as the mean value of the first 100 samples of the 1st measurement and removed the value for evaluation. Then, root mean squared error (RMSE) and correlation coefficient ($\rho$) between measured angles with sensors and reference values were calculated for evaluating measurement accuracy. In this paper, inclination angles of lower limb segments in the sagittal plane were evaluated.

*4.1. Measurement of Lower Limb Angles in Treadmill Walking.* For the variable-Kalman-gain methods, values of the noise ratio $n$ and threshold values were determined by trial and error as shown below.

Method 3 (variable-gain method based on acceleration magnitude)

$$n = 10^4, \quad \text{for } |\alpha| \leq 20 \text{ mG},$$
$$n = 10^6, \quad \text{for } 20 \text{ mG} < |\alpha| \leq 300 \text{ mG},$$
$$n = 10^8, \quad \text{for } 300 \text{ mG} < |\alpha| \leq 1 \text{ G}, \qquad (9)$$
$$n = 10^{13}, \quad \text{for } 1 \text{ G} < |\alpha|.$$

Method 4 (variable-gain method based on angle error)

$$n = 10^4, \quad \text{for } |\hat{\theta} - \theta_{acc}| \leq 1 \text{ deg},$$
$$n = 10^6, \quad \text{for } 1 \text{ deg} < |\hat{\theta} - \theta_{acc}| \leq 15 \text{ deg},$$
$$n = 10^8, \quad \text{for } 15 \text{ deg} < |\hat{\theta} - \theta_{acc}| \leq 60 \text{ deg}, \qquad (10)$$
$$n = 10^{13}, \quad \text{for } 60 \text{ deg} < |\hat{\theta} - \theta_{acc}|.$$

Here, the cutoff frequency of the low-pass filter for acceleration signals $f_c$ was 10 Hz for both methods.

Figures 3 and 4 show RMSE values and $\rho$ values of measured inclination angles, respectively. The proposed variable-gain method (Method 4) showed the smallest average RMSE

(a) Foot inclination angle



(b) Shank inclination angle
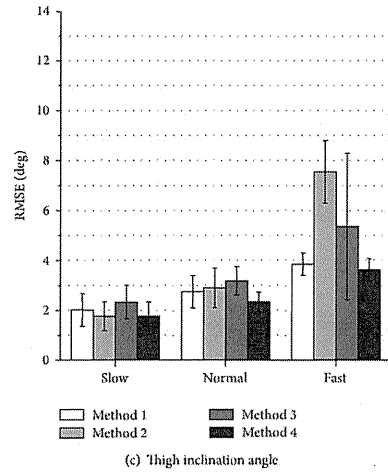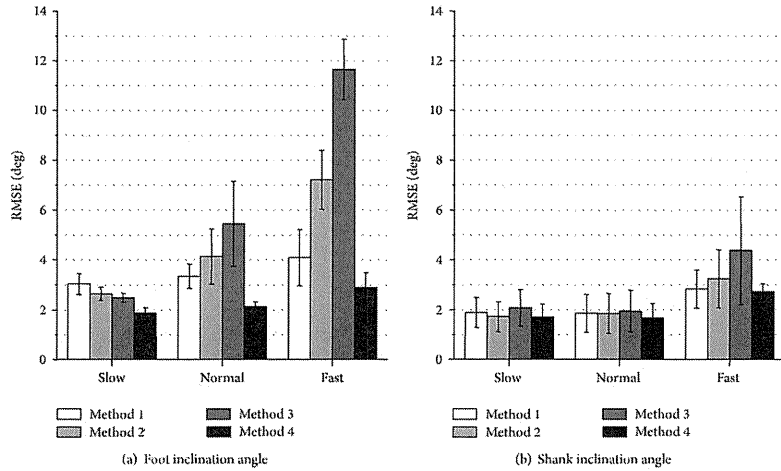


(c) Thigh inclination angle
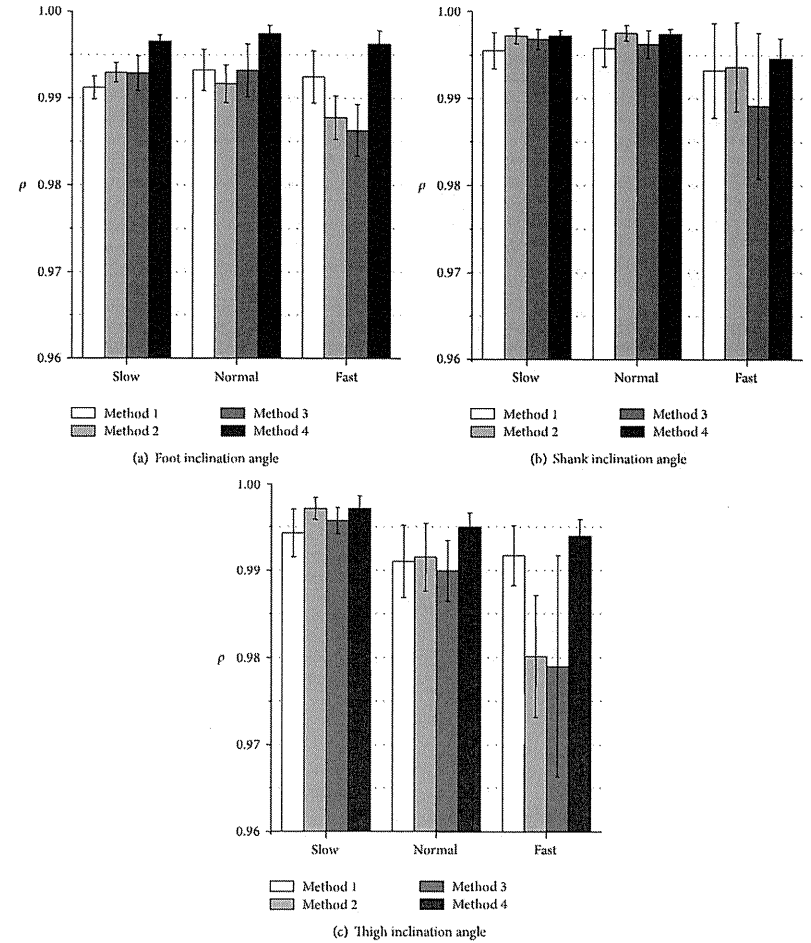
FIGURE 3: Evaluation results of RMSE of measured inclination angles during treadmill walking. Average values obtained from the results of 5 trials of all subjects are shown for each walking speed.

values and the largest $\rho$ values for all of measurement conditions. Method 4 achieved average RMSE values of less than 3.0 deg except for thigh angle at fast walking speed and average values of correlation coefficient larger than 0.994 for all the measurement conditions.

The measurement accuracy of foot inclination angle was improved significantly with Method 4 for all walking speeds comparing to the results of Method 1 used in our previous

studies (Figures 3(a) and 4(a)). For the shank and the thigh inclination angles, slight improvement of RMSE values and $\rho$ values was shown for all walking speeds with Method 4 compared to the results of Method 1 (Figures 3(b), 3(c) and 4(b), 4(c)).

The values of RMSE with Method 2 (fixed-gain method with higher cut-off frequency) decreased compared to the results of Method 1 in all the segments at slow walking

---

(a) Foot inclination angle



(b) Shank inclination angle



(c) Thigh inclination angle

FIGURE 4: Evaluation results of correlation coefficient ($\rho$) of measured inclination angles during treadmill walking. Average values obtained from the results of 5 trials of all subjects are shown for each walking speed.

speed. However, at normal and fast walking speeds, the values of RMSE with Method 2 increased compared to the results of Method 1. Method 3 (variable-gain method based on acceleration magnitude) reduced measurement accuracy especially for fast waking speed and for foot inclination angle.

*4.2. Measurement of Angles Using Rigid Body Model.* The parameter values used for Methods 3 and 4 are shown below.

Method 3 (variable-gain method based on acceleration magnitude)

$$n = 10^4, \quad \text{for } |\alpha| \le 10\,\text{mG},$$
$$n = 3 \times 10^6, \quad \text{for } 10\,\text{mG} < |\alpha| \le 200\,\text{mG},$$
$$n = 10^7, \quad \text{for } 200\,\text{mG} < |\alpha| \le 400\,\text{mG},$$
$$n = 2 \times 10^7, \quad \text{for } 400\,\text{mG} < |\alpha|.$$

(11)

(a) Shank inclination angle
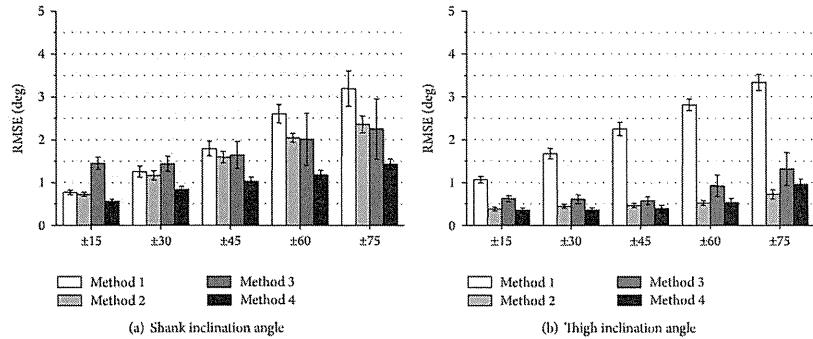
(b) Thigh inclination angle

FIGURE 5: Evaluation results of RMSE of measured inclination angles using rigid body model. Average values obtained from the results of 5 trials are shown for each target angle range.
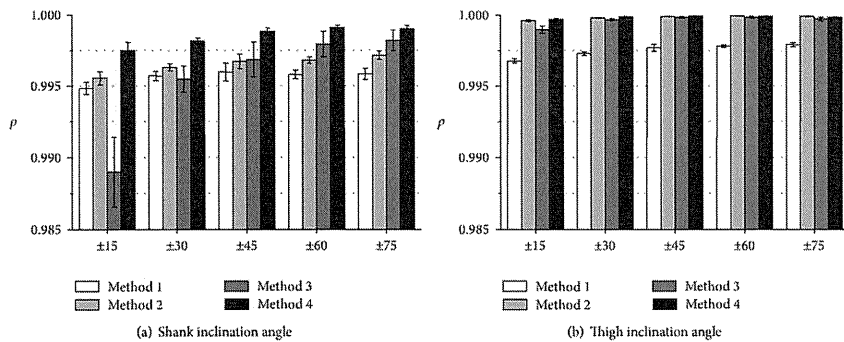


(a) Shank inclination angle

(b) Thigh inclination angle

FIGURE 6: Evaluation results of correlation coefficient ($\rho$) of measured inclination angles using rigid body model. Average values obtained from the results of 5 trials are shown for each target angle range.

Method 4 (variable-gain method based on angle error)

$$n = 10^4, \quad \text{for } |\hat{\theta} - \theta_{acc}| \leq 1 \text{ deg},$$
$$n = 3 \times 10^6, \quad \text{for } 1 \text{ deg} < |\hat{\theta} - \theta_{acc}| \leq 20 \text{ deg},$$
$$n = 10^7, \quad \text{for } 20 \text{ deg} < |\hat{\theta} - \theta_{acc}| \leq 30 \text{ deg}, \quad (12)$$
$$n = 2 \times 10^7, \quad \text{for } 30 \text{ deg} < |\hat{\theta} - \theta_{acc}|.$$

Here, the cutoff frequency of the low-pass filter for acceleration signals $f_c$ was 10 Hz for both methods. The parameter values of Methods 3 and 4 were changed from those values in

angle measurement with human subjects, since magnitude of impact and motion acceleration signals and angle difference $|\hat{\theta} - \theta_{acc}|$ were smaller than that in the measurement with human subjects.

Figures 5 and 6 show RMSE values and $\rho$ values of measured inclination angles, respectively. The proposed variable-gain method (Method 4) showed highest measurement accuracy almost for all the target angle ranges. Average values of RMSE and correlation coefficient with Method 4 were less than 1.5 deg and larger than 0.9975, respectively. Although Methods 2 and 3 were also effective to improve measurement accuracy, Method 3 could not improve shank angle in movements of target angle range of ±15 deg and ±30 deg.
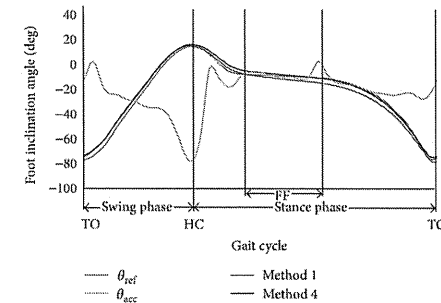
Gait cycle

FIGURE 7: An example of waveforms of reference and measured foot inclination angles at normal walking speed. $\theta_{ref}$ and $\theta_{acc}$ represent reference angle and angle calculated from acceleration signals, respectively. The x-axis shows the gait cycle. The toe off, the heel contact, and the foot flat are represented by TO, HC, and FF, respectively.

## 5. Discussion

The proposed variable-Kalman-gain method (Method 4) measured lower limb angles in treadmill walking with the smallest average values of RMSE and the largest average values of correlation coefficient. In particular, Method 4 showed significant improvement in calculation of foot inclination angle in treadmill walking compared to our previous method (Method 1). It is a useful result that measurement accuracy of foot inclination angle was improved, because evaluation of foot movements in walking is important for gait of motor disabled subjects and elderly persons. In measurement of shank and thigh angles, values of the noise ratio were not so greatly varied, since magnitude of the angle difference $|\hat{\theta} - \theta_{acc}|$ did not fluctuate significantly during movements. This is one of the reasons why improvement of measurement accuracy was not so large in shank and thigh angles with Method 4.

The proposed variable-Kalman-gain method (Method 4) was highly effective in calculation of foot inclination angle. Figure 7 shows the reference and calculated foot inclination angles of one gait cycle at normal walking speed. As seen in Figure 7, the calculated angle with Method 4 was almost equal to that with Method 1 between around the TO and the HC in the swing phase. Method 4 improved angle calculation between around the FF and the TO in the stance phase. It is considered that the sensor attached on the foot was close to the stationary state at around the FF. At that time, the variable-Kalman-gain method corrected the angle significantly increasing values of Kalman gain (decreasing noise ratio), since the angle difference $|\hat{\theta} - \theta_{acc}|$ was small as the influence of impact and movement accelerations was small. It is possible to decrease angle measurement error between the FF and the TO by reducing noise ratio with Method 1. However, in that case, angle error between around the TO and the HC is increased by the influence of impact and movement accelerations. Method 4 reduced Kalman gain

effectively at around the TO and the HC, since the angle difference $|\hat{\theta} - \theta_{acc}|$ increased. Therefore, the Method 4 could be effective especially in foot angle measurement, decreasing the influence of impact and motion accelerations.

As shown in Figure 3, RMSE values of measured inclination angles in treadmill walking with Method 2 decreased at slow walking speed compared to the results of Method 1 in all segments. In addition, as shown in Figure 5, RMSE values of measured inclination angles of the rigid body model with Method 2 decreased at all target angle ranges compared to the results of Method 1 for both segments. These suggest that very low cutoff frequency for the low-pass filtering of the acceleration signal increases measurement error if impact and movement accelerations are not so large. The cause of error increases in treadmill walking at the normal and fast walking speeds with Method 2 is considered to be influences of impact and motion accelerations. It is considered that although 0.5 Hz of cutoff frequency is reasonable value for removing impact and motion accelerations in angle calculation of human gait, error increase is caused by the large delay in the low pass filtering.

The variable-gain method based on acceleration magnitude (Method 3) did not show improvement of measurement accuracy of lower limb angles of human gait. For most of measurement conditions, average values of RMSE increased, and those of correlation coefficient decreased. The parameter values that are good for changing Kalman gain used in (9)–(12) were determined by trial and error method for both variable-gain methods. Although there is a possibility of improving measurement accuracy with Methods 3 and 4, the results of this paper suggest that the proposed method of changing the Kalman gain based on angle error was more suitable to the Kalman filter used in our system than that based on acceleration magnitude.

In angle measurement of the rigid body model, the values of RMSE with Method 4 were less than 1.5 deg for all segments and all target angle ranges. Those RMSE values

(a) Foot inclination angle

(b) Shank inclination angle
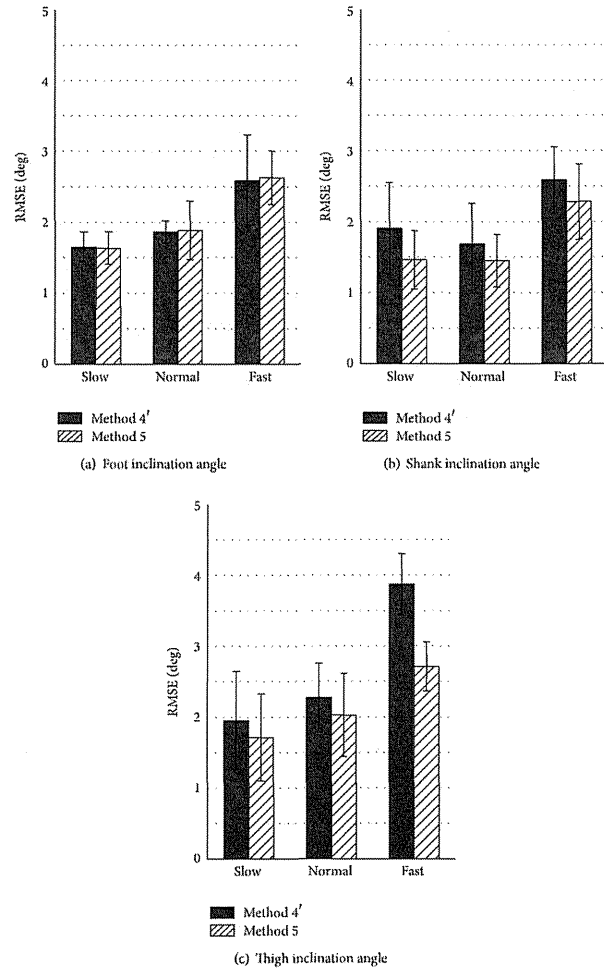


(c) Thigh inclination angle

FIGURE 8: Average values of RMSE of measured inclination angles during treadmill walking calculated by using Methods 4 and 5.

show measurement accuracy similar to or higher than results seen in other studies that used markers of camera-based motion measurement system fixing on a rigid plate together with the sensor or on the sensor directly [4, 8, 10, 11]. It is considered that the proposed variable-gain method became effective in measurement of human gait.

In the proposed variable-gain method, influence of impact and motion accelerations was approximately represented by $|\hat{\theta} - \theta_{acc}|$. Here, the approximation was validated by comparing to results of using $|\theta_{ref} - \theta_{acc}|$ as shown in Figure 8, in which $\theta_{ref}$ shows reference value measured with the camera-based motion measurement system. In the

---
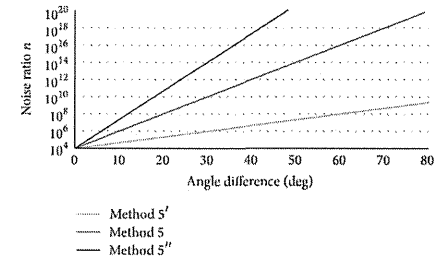
FIGURE 9: Relationships between the noise ratio and the angle difference used in the test of influence of the noise ratio.

comparison, the noise ratio (Kalman gain) was determined as continuous value by the followings from the angle difference. Method 4':

$$n = 10^4 e^{0.46 \cdot |\hat{\theta} - \theta_{acc}|}.$$ (13)

Method 5:

$$n = 10^4 e^{0.46 \cdot |\theta_{ref} - \theta_{acc}|}.$$ (14)

Here, (13) and (14) were derived by linear approximation of discrete values of the noise ratio $n$ in (10). That is,

$$\log n = ax + \log b,$$ (15)

where $a$ and $b$ represent constant values and $x$ represents the angle difference. The constant value $a$ was determined to decrease RMSE values by trial and error method, and $b$ was set $10^4$ from (10). As shown in Figure 8, for foot inclination angles, measurement results with Method 5 were similar to the results with Method 4' for all walking speeds. Measurement results for the shank and the thigh inclination angles were improved for all walking speeds with Method 5 using reference values. Average values of RMSE with Method 5 were less than 3.0 deg for all walking speeds and all segments. This result suggests that the proposed variable-Kalman-gain method based on angle error is effective to improve measurement accuracy of angle during human gait. It is also suggested that measurement accuracy with Method 4' can be improved if error in $|\hat{\theta} - \theta_{acc}|$ is reduced.

Angle measurement accuracy depends on the noise ratio. In this paper, parameter values to calculate values of noise ratio used in (9)–(14) were determined to decrease RMSE values by trial and error method. Here, different relationships between the noise ratio and the angle difference described by (14) were examined. Figures 9 and 10 show the tested relationships and results of their measurement accuracy, respectively. Method 5' used smaller noise ratio and Method 5'' used larger noise ratio than Method 5. In Figure 10, the results obtained by Method 1 (fixed-gain method) are also shown. The RMSE values were decreased with variable-gain

method in any parameter setting compared to the fixed-gain method. However, Method 5' (smaller noise ratio) showed larger RMSE values than Method 5 for all the measurement conditions. It is considered that the influence of impact and movement accelerations was not decreased sufficiently with Method 5' because of large value of Kalman gain (small noise ratio). On the other hand, RMSE values with Method 5'' (larger noise ratio) were similar to that of Method 5 for almost all the measurement conditions. However, Method 5'' has a tendency to increase RMSE values of the thigh and the shank inclination angles for the fast walking speed. Therefore, further studies on the method to determine appropriate Kalman gain are expected. In addition, this paper focused only on the error of angle calculated from acceleration signals in determination of Kalman gain. It is considered that the noise ratio also depends on magnitude of the offset drift of gyroscope. This is also required to be studied more for measurement of angles with the variable-gain Kalman filter. Finally, the proposed variable-Kalman-gain method was validated in measurement of inclination angles of lower limb segments in the sagittal plane in this paper. It is expected to show the effectiveness of the proposed method in measurement of 3 dimensional angles.

## 6. Conclusion

In this paper, variable-gain Kalman filter was tested to improve measurement accuracy of lower limb angles during gait, in which two calculation methods of Kalman gain were compared to fixed-gain Kalman filter. In measurements of lower limb angles of healthy subjects in treadmill walking and that of angles of a rigid body model, the variable-gain method based on the angle difference proposed in this study showed the highest measurement accuracy for most of measurement conditions. In particular, the proposed variable-gain method improved significantly measurement accuracy of foot inclination angle in human gait. On the other hand, measurement results of the shank and the thigh inclination angles show slight improvement of measurement accuracy. The proposed variable-gain method was found to be effective in angle measurement with inertial sensors. The

(a) Foot inclination angle



(b) Shank inclination angle
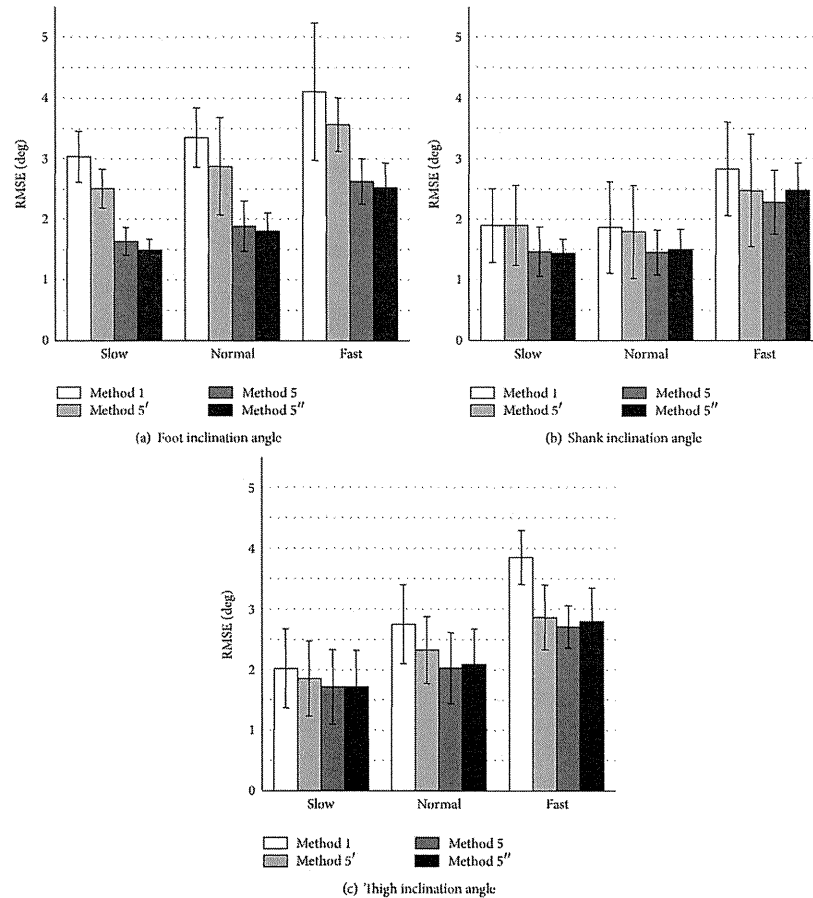


(c) Thigh inclination angle

FIGURE 10: Average RMSE values of measured inclination angles during treadmill walking calculated by fixed-gain method (Method 1) and variable-gain method with 3 different parameter settings for the noise ratio.

results also suggested that more accurate measurement can be realized by improving estimation accuracy of the angle difference $|\theta_{ref} - \theta_{acc}|$. Further studies on this point and to find appropriate method to determine Kalman gain using the angle difference and other parameters are expected.

## Acknowledgment

## References

[1] K. Tong and M. H. Granat, "A practical gait analysis system using gyroscopes," *Medical Engineering and Physics*, vol. 21, no. 2, pp. 87–94, 1999.

[2] H. Dejnabadi, B. M. Jolles, and K. Aminian, "A new approach to accurate measurement of uniaxial joint angles based on a combination of accelerometers and gyroscopes," *IEEE Transactions on Biomedical Engineering*, vol. 52, no. 8, pp. 1478–1484, 2005.

[3] J. C. Alvarez, R. C. González, D. Alvarez, A. M. López, and J. Rodríguez-Uría, "Multisensor approach to walking distance estimation with foot inertial sensing," in *Proceedings of the 29th Annual International Conference of IEEE-EMBS, Engineering in Medicine and Biology Society (EMBC '07)*, pp. 5719–5722, August 2007.

[4] D. Roetenberg, P. J. Slycke, and P. H. Veltink, "Ambulatory position and orientation tracking fusing magnetic and inertial sensing," *Transactions on Biomedical Engineering*, vol. 54, no. 5, pp. 883–890, 2007.

[5] S. J. M. Bamberg, A. Y. Benbasat, D. M. Scarborough, D. E. Krebs, and J. A. Paradiso, "Gait analysis using a shoe-integrated wireless sensor system," *IEEE Transactions on Information Technology in Biomedicine*, vol. 12, no. 4, pp. 413–423, 2008.

[6] A. Findlow, J. Y. Goulermas, C. Nester, D. Howard, and L. P. J. Kenney, "Predicting lower limb joint kinematics using wearable motion sensors," *Gait and Posture*, vol. 28, no. 1, pp. 120–126, 2008.

[7] R. Takeda, S. Tadano, A. Natorigawa, M. Todoh, and S. Yoshinari, "Gait posture estimation using wearable acceleration and gyro sensors," *Journal of Biomechanics*, vol. 42, no. 15, pp. 2486–2494, 2009.

[8] M. D. Djurić-Jovičić, N. S. Jovicic, D. B. Popović, and A. R. Djordjević, "Nonlinear optimization for drift removal in estimation of gait kinematics based on accelerometers," *Journal of Biomechanics*, vol. 45, no. 16, pp. 2849–2854, 2012.

[9] C. Mazzà, M. Donati, J. McCamley, P. Picerno, and A. Cappozzo, "An optimized Kalman filter for the estimate of trunk orientation from inertial sensors data during treadmill walking," *Gait and Posture*, vol. 35, no. 1, pp. 138–142, 2012.

[10] B. J. E. Misgeld, D. Ruschen, S. Kim, and S. Leonhardt, "Body sensor network-based strapdown orientation estimation: application to human locomotion," in *International Conference on Rehabilitation Robotics (ICORR '13)*, 2013.

[11] A. Caroselli, F. Bagala, and A. Cappello, "Quasi-real time estimation of angular kinematics using single-axis accelerometers," *Sensors*, vol. 13, no. 1, pp. 918–937, 2013.

[12] J. M. Jasiewicz, J. H. J. Allum, J. W. Middleton et al., "Gait event detection using linear accelerometers or angular velocity transducers in able-bodied and spinal-cord injured individuals," *Gait and Posture*, vol. 24, no. 4, pp. 502–509, 2006.

[13] H. Lau and K. Tong, "The reliability of using accelerometer and gyroscope for gait event identification on persons with dropped foot," *Gait and Posture*, vol. 27, no. 2, pp. 248–257, 2008.

[14] H. Saito and T. Watanabe, "Kalman-filtering-based joint angle measurement with wireless wearable sensor system for simplified gait analysis," *IEICE Transactions on Information and Systems*, vol. 94, no. 8, pp. 1716–1720, 2011.

[15] T. Watanabe and H. Saito, "Tests of wireless wearable sensor system in joint angle measurement of lower limbs," in *Proceedings of the 33rd Annual International Conference of the IEEE Engineering in Medicine and Biology Society (EMBS '11)*, pp. 5469–5472, September 2011.

[16] A. M. Sabatini, "Quaternion-based extended Kalman filter for determining orientation by inertial and magnetic sensing," *IEEE Transactions on Biomedical Engineering*, vol. 53, no. 7, pp. 1346–1356, 2006.

**CALL FOR PAPERS** | *Bioengineering the Lung: Molecules, Materials, Matrix, Morphology, and Mechanics*

# Fluctuation of cilia-generated flow on the surface of the tracheal lumen

Kouki Kiyota,[1] Hironori Ueno,[2] Keiko Numayama-Tsuruta,[1] Tomofumi Haga,[1] Yohsuke Imai,[3] Takami Yamaguchi,[1] and Takuji Ishikawa[1,3]

[1]*Department Biomedical Engineering, Graduate School of Biomedical Engineering, Tohoku University, Aoba, Aramaki, Aoba-ku, Sendai, Japan;* [2]*Faculty of Education, Aichi University of Education, Hirosawa, Igaya-cho, Kariya, Aichi, Japan; and* [3]*Department Bioengineering and Robotics, Graduate School of Engineering, Tohoku University, Aoba, Aramaki, Aoba-ku, Sendai, Japan*

Kiyota K, Ueno H, Numayama-Tsuruta K, Haga T, Imai Y, Yamaguchi T, Ishikawa T. Fluctuation of cilia-generated flow on the surface of the tracheal lumen. *Am J Physiol Lung Cell Mol Physiol* 306: L144–L151, 2014. First published November 6, 2013; doi:10.1152/ajplung.00117.2013.—Although we inhale air that contains many harmful substances, including, for example, dust and viruses, these small particles are trapped on the surface of the tracheal lumen and transported towards the larynx by cilia-generated flow. The transport phenomena are affected not only by the time- and space-average flow field but also by the fluctuation of the flow. Because flow fluctuation has received little attention, we investigated it experimentally in mice. To understand the origin of flow fluctuation, we first measured the distribution of ciliated cells in the trachea and individual ciliary motions. We then measured the detailed flow field using a confocal micro-PTV system. Strong flow fluctuations were observed, caused by the unsteadiness of the ciliary beat and the spatial inhomogeneity of ciliated cells. The spreading of particles relative to the bulk motion became diffusive if the time scale was sufficiently larger than the beat period. Finally, we quantified the effects of flow fluctuation on bulk flow by evaluating the Peclet number of the system, which indicated that the directional transport was an order of magnitude larger than the isotropic diffusion. These results are important in understanding transport phenomena in the airways on a cellular scale.

cilia; fluid mechanics; mixing; particle tracking velocimetry; transport phenomena

WHEN WE INHALE AIR TO OBTAIN oxygen, we sometimes also inhale small particles, such as viruses, bacteria, pollen, and dust. These particles are trapped on the surface of the tracheal lumen and transported towards the larynx by cilia-generated mucous flow, known as the clearance function. If the clearance function does not work properly, harmful substances may remain in the body and may cause various diseases and infections, such as pneumonia and influenza (1, 7, 10, 16–19).

The clearance function has been investigated from many points of view. In 1934, Lucas and Douglas (14) reported the presence of two fluid layers on the epithelium of the trachea. A periciliary layer (PCL) exists on the epithelial cells and has low viscosity, while a mucus layer (ML) exists on top of the PCL

and has a much higher viscosity than that of the PCL. The classical picture of the two-layer structure was recently modified by Button et al. (4), so that the PCL is not just a watery fluid but contains membrane-spanning mucins and mucopolysaccharides. It is also known that cilia of the tracheal lumen show two kinds of strokes, an effective stroke and a recovery stroke, with a frequency of about 10–20 Hz (6, 20, 22, 27, 28). Due to the asymmetry of the strokes, the cilia generate a net flow towards the larynx (23, 27).

Velocity analyses of cilia-generated flow have been performed both experimentally and numerically (8, 12, 15, 24–26). Hussong et al. (8) clarified the time-averaged flow structure around epithelial cells and discussed the effect of ATP stimulation on particle transport. These former studies are important in understanding the time- and space-average flow field; however, the time and space fluctuations of the flow have received little attention to date. Flow fluctuation is one of the key quantities in particle transport, given that transport phenomena are governed by advection, due to the bulk flow, and diffusion, due to flow fluctuations and Brownian motion.

In this study, we investigated the time and space fluctuations of cilia-generated flow experimentally in mice. To understand the origin of flow fluctuation, we first measured the distribution of ciliated cells in the trachea and their ciliary motion. Next, we measured the in-plane flow field at different heights of observation using a confocal micro-PTV system. This system enabled us to accurately measure the flow with high resolution in time and space. Finally, we quantified the effect of flow fluctuation on bulk flow by evaluating the Peclet number (cf. *Eqs. 7* and *2*) of the system.

## MATERIALS AND METHODS

*Preparation of samples.* Experiments were conducted with approval by the Animal Ethics Review Board of Tohoku University. Figure 1 illustrates the procedure for sample preparation. Tracheas were obtained exclusively from wild-type mice (Crlj:CD1), 4–16 wk old. The mice were killed by cervical dislocation. The trachea was then dissected from the larynx to the bronchial main branches and doused with L-15 medium (GIBCO) + 10% fetal bovine serum (FBS; Thermo Scientific). Muscle and vascular tissues were removed from the trachea in cold medium. The trachea was opened longitudinally, and 3-mm square specimens were excised. The exposed tracheal lumens were soaked in L-15 medium including 5 mM dithiothreitol (DTT; Fluka) to gently remove the original mucus and contaminating
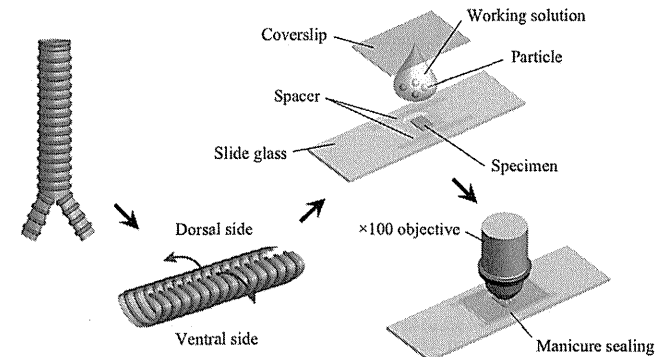


Fig. 1. Schematic of the experimental procedure. A trachea was excised by dissection, and a specimen of about 3 × 3 mm was placed between the slide glass and the coverslip.

impurities during the preparation process. After incubating in L-15 medium with DTT, the specimens were washed with L-15 + 10% FBS. Then, we added a drop of working solution including fluorescent particles. When we measured the flow field, tracers of 1-μm diameter were used to minimize the effect of Brownian motion while maintaining high resolution. When we measured ciliary motion, on the other hand, tracers of 0.5-μm diameter were used to reduce the viscous drag caused by the tracer. The specimen was placed on a slide glass and covered by a coverslip (Matsunami), in which two spacers prevented the specimen from being pressed directly. The distance between the coverslip and the slide glass was ~100 μm, and the gap at the edge was sealed. Curved air-liquid interfaces may generate inhomogeneity in surface tension and Marangoni stress at the inter-

face, leading to complex flow. To avoid such uncertainty and to measure the flow field precisely, we used a coverslip.

*Experimental setup.* When we measured the flow field, a confocal micro-PTV system was used, similar to that in our former studies (13, 21) but with an upright instead of an inverted microscope. Figure 2 shows a schematic of the system used, consisting of a fluorescence upright microscope (BX51WI; Olympus), a Nipkow lens-type confocal unit (CSU-X1; Yokogawa), a high-speed camera (SA3; Photron), and a ×100 objective lens (Olympus). The observation height was controlled by a piezo actuator (E-665; PI). The temperature of the sample was regulated at 37°C using a thermo plate (MATS-55RAF20; Tokai Hit). When we measured ciliary motion, we also used another setup, consisting of a fluorescent microscope (DM4000B; Leica), a
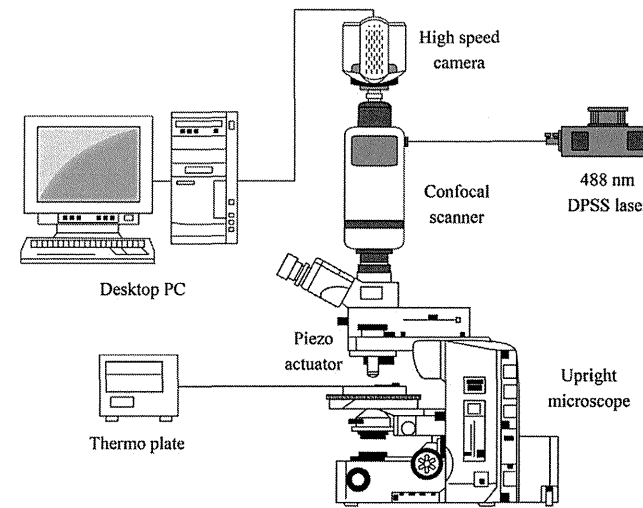


Fig. 2. Experimental setup of the confocal micro-PTV system.

Address for reprint requests and other correspondence: T. Ishikawa, Dept. of Bioengineering and Robotics, Graduate School of Engineering, Tohoku Univ., 6-6-01, Aoba, Aramaki, Aoba-ku, Sendai 980-8579, Japan (e-mail: ishikawa@pfsl.mech.tohoku.ac.jp).

mercury lamp (ebq 100; LEj), and a high-speed camera (HAS-220; Ditect).

*Cell staining.* We performed phalloidin staining for visualization of actin filaments and immunofluorescent staining of respiratory cilia using anti-acetylated tubulin antibody, according to Francis et al. (6). For immunostaining, tracheas were fixed in 4% paraformaldehyde and then permeabilized with PBST (0.2% Triton in PBS), blocked with buffer (5% goat serum + 0.1% Triton in PBS), and incubated overnight at 4°C with a monoclonal anti-acetylated tubulin antibody (Sigma). Then, fluorescent labeling was achieved with an Alexa Fluor 532-conjugated anti-mouse IgG as the secondary antibody, diluted in PBST2 (×500, 0.1% Triton in PBS), and Alexa Fluor 488-conjugated phalloidin, diluted in PBST2 (×40). The tissues were imaged using the Leica microscope with a ×100 oil immersion objective lens. In total, 26 locations were selected randomly, and an area of 128 × 96 μm was recorded at each location. Images of epithelial cells and cilia were taken, colored separately, and merged using Adobe Photoshop CS4 (Adobe Systems).

*Analysis of ciliary beat.* Cilia were labeled individually with a polystyrene tracer particle of 0.5-μm diameter (wavelength 505 nm; Molecular Probes) by nonspecific binding to facilitate visualization of ciliary motion. The claw-like structures called ciliary crown is elongated from the surface of the ciliary tip (5), to which we intend to bond the tracer particles. The sample was washed before the experiment to remove nonbinding tracer particles. The motions of tracer particles were tracked at 200 frames/s in bright-field images. Oscillation of each tracer particle was analyzed along the beat axis e (see Fig. 3B and Supplemental Movie S1; Supplemental Material for this article is available online at the *Am J Physiol Lung Cell Mol Physiol* website), and the time history of the tracer oscillation along the beat axis was plotted (Fig. 3C) using the ImageJ software (National Institutes of Health). After a time history of tracer oscillation had been obtained, the beat frequency (BF) could be calculated readily by counting the peaks during a 1-s period. The velocity of effective and recovery strokes were defined as the slopes at the crossing points of the line of average e value (Fig. 3D). The velocities of effective strokes are shown as the slopes of the dashed lines; i.e., from the bottom of the figure (lung side) to the top (larynx side). The velocities of recovery strokes are shown as slopes of the chain lines; i.e., from the top of the figure (larynx side) to the bottom (lung side).

*Analysis of cilia-generated flow.* For flow visualization, fluorescent polystyrene beads of 1-μm diameter (wavelength: 505 nm; Molecular

Probes) were coated with bovine serum albumin (BSA; Sigma) to prevent nonspecific binding to tissue surfaces and then added to the working solution. The trajectories of particles were recorded using the confocal micro-PTV system at a frame rate of 60 frames/s. The observation plane was controlled by the piezo actuator. The observation height *H* was measured from the plane of the tips of the cilia, and particle motions in the planes with $H = 0, 5, 10, 15$, and 20 μm were measured. We note that the focal plane thickness is ~0.7 μm in the present setup. In each movie, motions of five particles during an at least 1-s period were analyzed using the ImageJ software.

Let the velocity of particle *i* at time *t* be $v_i(t)$, and the time-average velocity of particle *i* be $\bar{v}_i$. Flow fluctuation may be quantified by calculating the standard deviation of the velocity (SDV). We, thus, calculated the SDV of each bead in the parallel and the normal directions to $\bar{v}_i$, i.e., $SDV_{bead,para}$ and $SDV_{bead,norm}$ given by:

$$SDV_{bead,para} = \sqrt{\frac{1}{N_p N_f} \sum_{i=1}^{N_p} \sum_{k=1}^{N_f} [v_{i,para}(k\Delta t) - \bar{v}_i]^2}, \quad (1)$$

$$SDV_{bead,norm} = \sqrt{\frac{1}{N_p N_f} \sum_{i=1}^{N_p} \sum_{k=1}^{N_f} [v_{i,norm}(k\Delta t)]^2}, \quad (2)$$

where $N_p$ is the total number of particles, $N_f$ is the total number of frames, $v_{i,para}$ and $v_{i,norm}$ are the parallel and the normal components of $v_i$, and $\Delta t$ is the time interval between two successive images. $SDV_{bead}$ indicates how an individual bead fluctuates relative to its time-average motion.

It is also important to discuss how each bead fluctuates relative to the particle-average motion. We, thus, calculated the particle-average velocity in each movie and define $SDV_{mov}$ as:

$$SDV_{mov} = \sqrt{\frac{1}{5N_m} \sum_{m=1}^{N_m} \sum_{i=1}^{5} [\bar{v}_{i,m} - V_m]^2}, \quad (3)$$

where $N_m$ is the number of movies, $\bar{v}_{i,m}$ is the time-average velocity of particle *i* in movie *m*, and $V_m$ is the average $\bar{v}_{i,m}$ of five particles in movie *m*. $SDV_{mov}$ indicates the fluctuation in time-average motion of an individual bead relative to the bulk motion of beads in the movie. Furthermore, we analyzed the deviation angle of the $\bar{v}_{i,m}$ vector from the $V_m$ vector, defined as:
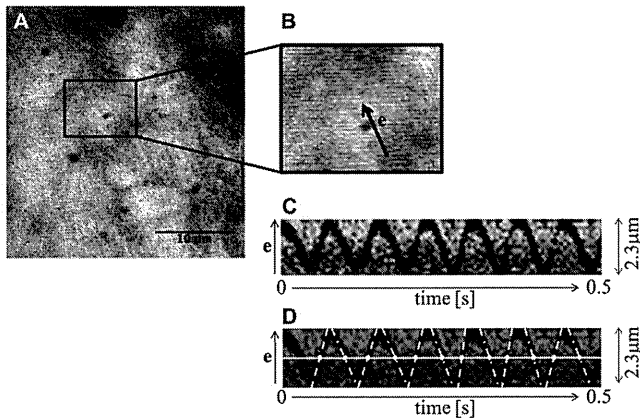


Fig. 3. Analysis of ciliary beat. *A*: observation of tracer particles attached to the tips of cilia (bright field). *B*: magnified image of *A*, where e is the beat axis (see also Supplemental Movie S1). *C*: time history of the tracer motion during 0.5 s. *D*: slope indicates the velocity of the ciliary beat. The velocity of the effective stroke is shown as the slope of dashed lines, whereas that of the recovery stroke is shown as the slope of chain lines.
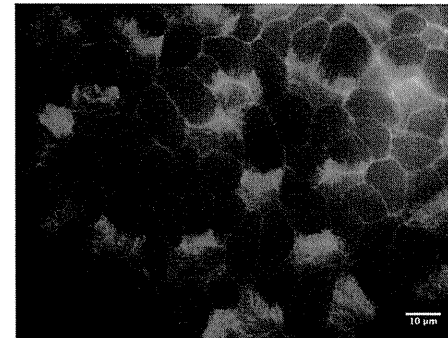
252

---

Fig. 4. Sample cell staining image. Cell morphologies were visualized by phalloidin staining of actin (green), while cilia were visualized by immunofluorescence analysis of acetylated-tubulin (red).

$$\text{deviation angle} = \frac{1}{5N_m} \sum_{m=1}^{N_m} \sum_{i=1}^{5} \arccos\left(\frac{\bar{v}_{i,m} \cdot V_m}{|\bar{v}_{i,m}| |V_m|}\right). \quad (4)$$

The deviation angle is defined in the range 0 to 180°. When all particles move in the same direction it is 0°, while when particle motion is almost random, it becomes 90°. Thus the deviation angle indicates the fluctuation in the flow direction.

*Analysis of particle spreading.* To quantify the spreading of particles relative to the bulk motion, we calculated the dispersion coefficient, defined as:

$$D' = \frac{\langle R^2 \rangle}{4k\Delta t}, \quad (5)$$

where $k\Delta t$ is the time interval. $R_i$ is the position vector of bead *i* relative to the bulk motion, defined as:

$$R_i(k\Delta t) = \int_0^{k\Delta t} [v_{i,m}(t) - V_m(t)]dt. \quad (6)$$

$\langle R^2 \rangle$ is the ensemble average of the square displacements relative to the bulk motion. By making the time interval sufficiently large, $D'$ may converge to the well-known diffusion coefficient if the spreading process can be described as a diffusion process.

Once the dispersion coefficient is obtained, we can define the Peclet number (Pe) as (2):

$$Pe = \frac{VL}{D'}, \quad (7)$$

where *V* is the characteristic velocity, and *L* is the characteristic length. Pe indicates the ratio of advection to diffusion. When Pe >> 1, mass transport is dominated by advection, and particles move with the bulk fluid motion. When Pe << 1, on the other hand, mass transport is dominated by diffusion. The particles diffuse similar to Brownian diffusion and background flow has little effect. Thus Pe is one of the most important dimensionless parameters in discussing mass transport.

## RESULTS AND DISCUSSION

*Distribution of ciliated cells.* Epithelial cells and cilia were stained separately (Fig. 4). We see that ciliated cells were not distributed homogeneously in the tracheal lumen but were distributed discretely at the cellular scale. Such inhomogeneity in the ciliated cell distribution is likely to induce flow fluctuations at the cellular scale.

The ratio of ciliated cells to all cells was also calculated from the stained images. It was found that the ratio of ciliated cells was about $36.7 \pm 9.6\%$ ($n = 26$, where *n* is the number of samples). This value is similar to that reported by Francis et al. (6). We note that the ratio changes not only with individual mice but also with the observation region of a single specimen, such as the annular ligament region, tracheal cartilage region, larynx side, or lung side. Such inhomogeneity may have lead to the ratio standard deviation of 9.6%. The ciliated cell distribution is thus inhomogeneous, even at a millimeter scale, and flow in the tracheal lumen could become inhomogeneous, not only on the cellular scale, but also on the millimeter scale.

*Ciliary beat.* We first show typical motions of particles that are attached to the tips of cilia (Fig. 5A and Supplemental Movie S2). The major axis e is calculated by image analysis (cf. Fig. 5B), and the motion of individual tracers in each e direction is shown in Fig. 5C. We see that all particles oscillate with similar amplitude, which indicates that the particles are attached at similar positions, i.e., at the tips of cilia. Supplemental Movie S2 also shows that particles other than the oscillating particles flow away from the frame. This fact illustrates that particles are not attached on the cell surface or
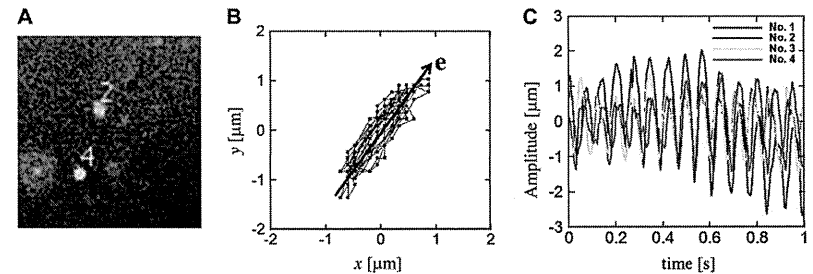


Fig. 5. Motion of tracers attached to the tips of cilia based on a same ciliary cell. *A*: number of tracked tracers attached to the tips of cilia (see also Supplemental Movie S2). *B*: trajectory of a tracer and its major axis e. *C*: motion of 4 tracers in each e direction.

particles attached on the cell surface are invisible due to the thin focal plane of our conforcal system.

We analyzed the BF by tracking a tracer particle attached to a cilium tip. The BF was about $11.8 \pm 6.4$ Hz ($n = 24$), showing good agreement with previous reports (20, 22, 27, 28). The deviation of beat direction e (cf. Fig. 3B) among four cilia in each movie was about $8.4 \pm 6.8°$. We then analyzed the velocities of the effective and recovery strokes. The velocity of the effective stroke was about $47.4 \pm 10.6$ μm/s ($n = 4$), while the velocity of the recovery stroke was about $28.6 \pm 5.8$ μm/s ($n = 4$). The effective stroke was ~1.7 times faster than the recovery stroke. Such reciprocal strokes generate oscillation of the flow on a time scale of ~100 ms. Combining the flow oscillation and the spatial inhomogeneity discussed above, cilia-generated flow in the tracheal lumen fluctuates strongly relative to the bulk steady flow.

*Cilia-generated flow.* We first tracked tracer particle motion at $H = 0$ μm in the fluorescent field, and then identified the positions of epithelial cells and cilia in the bright field at the same location. The results are shown in Fig. 6 (see also Supplemental Movie S3). We see that particles moved from the lungs side (Fig. 6, *bottom*) to the larynx side (Fig. 6, *top*), on average. The trajectories were not a straight line but erratic and unsteady. We consider that the fluctuations in the trajectories were caused by the reciprocal motion of the ciliary beat and the spatial inhomogeneity of ciliated cells.

The average velocity of all particles at each height of observation plane is shown in Fig. 7. The velocity was largest at the tip of cilia (i.e., $H = 0$ μm) at $13.8 \pm 8.6$ μm/s ($n = 20$). The velocity decays rapidly as the height increases, which may be explained in terms of fluid mechanics. The cilia-generated flow can be classified as Stokes flow, in which the viscous force is dominant and the inertial force is negligible. Stokes flow often appears in cellular-scale phenomena, because the system size is small enough to neglect body forces, such as the inertial force, compared with surface forces, such as the viscous force. In a Stokes flow regime, the velocity disturbance
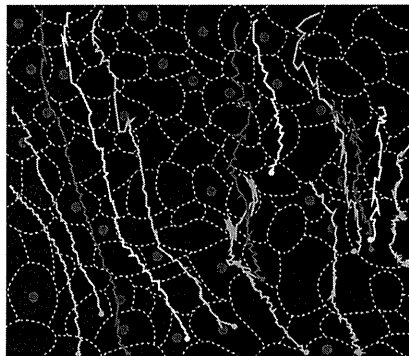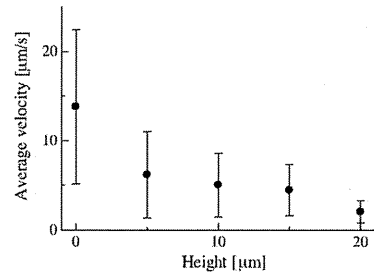


Fig. 7. Relationship between the average velocity and the height of the observation plane. $n = 20$ at each height, and the error bar indicates the SD.

induced by a point force near a wall decays rapidly as the distance from the wall increases (3). Because the flow observed in the present study satisfies the Stokes flow condition, the velocity induced by the force of the ciliary beat also decays rapidly with height from the ciliated cells. We note that the velocity distribution can be modified considerably by the boundary conditions. If a stress-free surface exists just above the cilia, we may not observe such decay in the velocity.

The velocity field may also be affected by rheological properties of the working solution. Lai et al. (11) reported that the viscosity of human mucus is about 0.1–1 Pa.s when the shear rate is about 100 s$^{-1}$. To clarify the effect of such high viscosity, we increased the viscosity of our working solution by adding methyl cellulose 400 (Wako Pure Chemical). The effect of viscosity on the flow velocity ($H = 0$ μm) and the BF of cilia is shown in Fig. 8. The horizontal axis is normalized by the viscosity of the original working solution, i.e., $1.2 \times 10^{-3}$ Pa·s, whereas the vertical axis is normalized by the velocity or the BF with the original working solution. We see that both velocity and BF decrease as the viscosity is increased. However, the velocity is still >20% even when the viscosity is increased up to 100 times. Similar tendency was also reported by Johnson et al. (9). These results illustrate that the effect of viscosity on the velocity is not significant, because the cilia
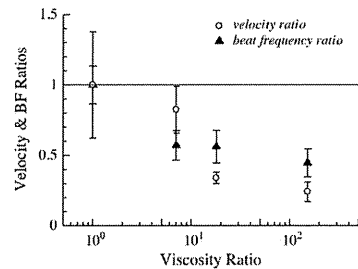


Fig. 8. The effect of viscosity on the flow velocity ($H = 0$ μm) and the beat frequency (BF) of cilia. The horizontal axis is normalized by the viscosity of working solution, i.e., $1.2 \times 10^{-3}$ Pa·s, whereas the vertical axis is normalized by the velocity or the BF with the working solution. The viscosity was increased by adding methyl cellulose.



Fig. 6. Trajectories of tracer particles at $H = 0$ μm. Borders of epithelial cells are shown by white dashed lines, and ciliated cells are indicated by red circles. Particle trajectories are shown by colored lines. Particles moved from the lungs side (*bottom*) to the larynx side (*top*), on average (see also Supplemental Movie S3).

---

tend to generate larger force when the viscosity is increased. We should note that real mucus is not only highly viscous but also viscoelastic. This effect was not investigated here due to experimental difficulties, which is a shortcoming of this study. We hope to address it in our future studies.

To discuss the flow disturbance, the standard deviation of the velocity (SDV) of each bead was calculated. SDV$_{bead,para}$ and SDV$_{bead,norm}$, defined by Eqs. 1 and 2, are plotted in Fig. 9 ($n = 20$ at each height). The dashed lines in the figure indicate the SDV of beads in the absence of ciliary flow ($n = 19$; i.e., pure Brownian motion). We see that SDV$_{bead,para}$ was significantly larger than the average velocity (cf. Fig. 7), meaning that the tracer particles do not move constantly in one direction but move erratically, back and forth, as seen in Fig. 6. SDV$_{bead,para}$ is considerably larger than SDV$_{bead,norm}$. This is because particles near the ciliated cells oscillate more in the flow direction, due to the reciprocal effective and recovery strokes. At $H = 0$ μm, the SDV was much larger than the dashed line of pure Brownian motion, indicating that the particles fluctuate mainly by the reciprocal motion of the ciliary beat and the spatial inhomogeneity of ciliated cells, and any effect of Brownian motion was small. At $H = 20$ μm, on the other hand, the SDV was only slightly larger than the dashed line, indicating that particles fluctuate strongly, also by Brownian motion. Thus the mechanism of the particle fluctuation changes with height.
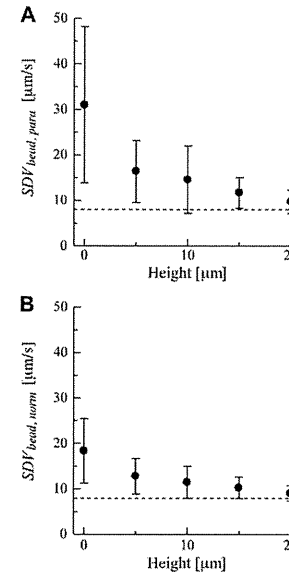


Fig. 9. Effect of height on the standard deviation of the velocity (SDV) of each bead. $n = 20$ at each height, and the error bar indicates the SD. Dashed lines indicate the SDV of beads in the absence of ciliary flow ($n = 19$; i.e., pure Brownian motion). A: parallel component to the time-average velocity of the bead SDV$_{bead,para}$; normal component to the time-average velocity of the bead SDV$_{bead,norm}$.
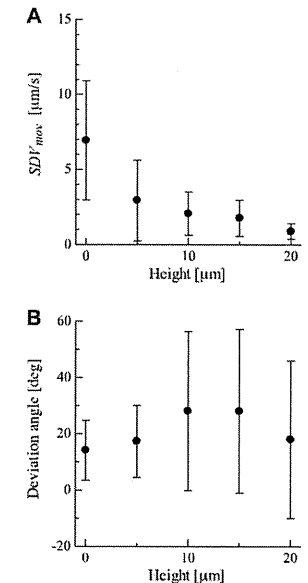


Fig. 10. Fluctuation of each bead motion relative to the particle-average motion; $n = 20$ at each height, and the error bar indicates the SD. A: relationship between SDV$_{mov}$ and height. B: relationship between deviation angle and height.

Although Fig. 9 clarifies how an individual bead fluctuates relative to its time-average motion, it is also important to discuss how each bead fluctuates relative to the particle-average motion. We thus calculated SDV$_{mov}$, defined by Eq. 3, and plotted it in Fig. 10A ($n = 20$ at each height). We see that SDV$_{mov}$ is about half of the average velocity shown in Fig. 7, indicating that each bead fluctuates strongly relative to the particle-average motion. Because the high-frequency oscilla-
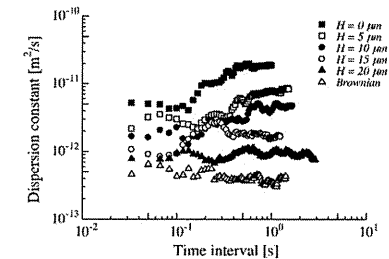


Fig. 11. Relationship between the dispersion constant, defined by Eq. 5, and the time interval at each height $H$ ($n = 20$ at each height). The results of pure Brownian motion (*Brownian*), in the absence of cilia-generated flow, are also plotted for comparison.

tion due to the ciliary beat has little effect in SDV$_{mov}$, we think the fluctuation is caused primarily by the spatial inhomogeneity of ciliated cells. We note that the difference of animal species may affect the results in some aspects, which should be clarified in future studies.

The direction of flow was not uniform in the observed area. We thus calculated the deviation angle, defined by Eq. 4, and plotted the results in Fig. 10B ($n = 20$ at each height). The deviation angle did not differ much with height, and the height-average value was ~21.1°. The fluctuation in the flow direction could be caused by inhomogeneity in the ciliary beat direction, so the ciliated cells are inhomogeneous, not only in physical space, but also in orientation space. Because the directional fluctuation was not too large, directional bulk flow could be developed, on average, from the lung side to the larynx side.

*Advection vs. diffusion.* Next, we quantified the spreading of particles relative to the bulk motion. The ensemble average of square displacements of beads relative to the bulk motion was calculated, and the dispersion coefficient $D'$, defined by Eq. 5, was obtained. The results are plotted in Fig. 11 at each height ($n = 20$ at each height). The results of pure Brownian motion (i.e., in the absence of cilia-generated flow) were also plotted in the figure for comparison. We see that the values of $D'$ converged well when the time interval was larger than ~0.5 s. In this time scale, the beads could experience several directional changes, because the BF of cilia was ~12 Hz. The beads lost directional memory and the spreading became diffusive. We can conclude that the spreading of particles, relative to bulk motion, becomes diffusive if the time scale is sufficiently larger than the beat period.

In Fig. 11, the values of $D'$ are significantly larger than Brownian diffusion. At $H = 0$ μm, for example, $D'$ is about two orders of magnitude larger than Brownian diffusion. These results indicate that the particles spread much intensively than by Brownian motion. Because the tracer particles move with the surrounding fluid, the mechanism of the enhanced diffusion can be explained by the flow fluctuations discussed above.

Once the dispersion coefficient is obtained, we can evaluate the Peclet number (Pe) of the system, which is the ratio of advection to diffusion, defined by Eq. 7. Here, we take the characteristic velocity $V$ as the average velocity at $H = 0$ μm (i.e., $V = 13.8$ μm/s) and the characteristic dispersion constant at $H = 0$ μm of $D' = 1.85 \times 10^{-11}$ m²/s. The characteristic length, $L$, is taken as the typical thickness of the mucous layer on the surface of tracheal lumen, and $L = 10$ μm is assumed. This is because the film thickness is usually taken as the characteristic length scale for film flow in the field of fluid mechanics. With the use of these values, the Pe of the system can be derived as 7.5. Because Pe is larger than unity, particles are transported more by advection than diffusion. This explains why tracer particles in the present study could be transported as a bulk even in the presence of such strong flow fluctuations.

*Conclusions.* In this study, we investigated the fluctuation of cilia-generated flow on the surface of the tracheal lumen. To understand the origin of flow fluctuation, we first measured the distribution of ciliated cells in the trachea and individual ciliary motions. The results indicated that the spatial distribution as well as the beat direction of ciliated cells were inhomogeneous. Next, we measured the in-plane flow field at different heights using a confocal micro-PTV system. The results showed that

the mean velocity and the velocity fluctuation decayed rapidly with increasing distance from the epithelial cells. Strong flow fluctuations were observed, caused by the reciprocal motion of the ciliary beat and the spatial inhomogeneity of ciliated cells. The spreading of particles relative to the bulk motion became diffusive if the time scale was sufficiently larger than the beat period. Finally, we quantified the effect of flow fluctuation on bulk flow by evaluating the Peclet number of the system. The results illustrated that ciliated cells could generate directional transport despite the large fluctuations caused by the reciprocal motion of the ciliary beat and the spatial inhomogeneity of ciliated cells. Pe = 7.5, indicating that the directional transport is one order of magnitude larger than the isotropic diffusion. These results are important for understanding the transport phenomena of airways on the cellular scale.

### GRANTS

### DISCLOSURES

### AUTHOR CONTRIBUTIONS

Author contributions: K.K., H.U., K.N.-T., and T.H. performed experiments; K.K., H.U., Y.I., and T.I. analyzed data; K.K., H.U., K.N.-T., Y.I., T.Y., and T.I. interpreted results of experiments; K.K. and T.I. prepared figures; K.K. and T.I. drafted manuscript; K.K., H.U., K.N.-T., Y.I., T.Y., and T.I. approved final version of manuscript; H.U., T.Y., and T.I. conception and design of research; T.I. edited and revised manuscript.

### REFERENCES

1. **Afzelius BA.** A human syndrome caused by immotile cilia. *Science* 193: 317–319, 1976.
2. **Bird RB, Stewart WE, Lightfoot EN.** *Transport Phenomena.* New York: John Wiley & Sons, 1960.
3. **Blake JR, Chwang AT.** Fundamental singularities of viscous flow. *J Eng Math* 8: 23–29, 1974.
4. **Button B, Cai LH, Ehre C, Kesimer M, Hill DB, Sheehan JK, Boucher RC, Rubinstein M.** A periciliary brush promotes the lung health by separating the mucus layer from airway epithelia. *Science* 337: 937–941, 2012.
5. **Dirksen ER, Satir P.** Ciliary activity in the mouse oviduct as studied by transmission and scanning electron microscopy. *Tissue Cell* 4: 389–403, 1972.
6. **Francis RJ, Chatterjee B, Loges NT, Zentgraf H, Omran H, Lo CW.** Initiation and maturation of cilia-generated flow in newborn and postnatal mouse airway. *Am J Physiol Lung Cell Mol Physiol* 296: L1067–L1075, 2009.
7. **Hirokawa N, Tanaka Y, Okada Y, Takeda S.** Nodal flow and the generation of left-right asymmetry. *Cell* 125: 33–45, 2006.
8. **Hussong J, Lindken R, Faulhammer P, Noreikat K, Sharp KV, Kummer W, Westerweel J.** Cilia-driven particle and fluid transport over mucus-free mice tracheae. *J Biomech* 46: 593–598, 2012.
9. **Johnson NT, Villalon M, Royce FH, Hard R, Verdugo P.** Autoregulation of beat frequency in respiratory ciliated cells. Demonstration by viscous loading. *Am Rev Respir Dis* 144: 1091–1094, 1991.
10. **Jonassen JA, Agustin JS, Follit JA, Pazour GJ.** Deletion of IFT20 in the mouse kidney causes misorientation of the mitotic spindle and cystic kidney disease. *J Cell Biol* 183: 377–384, 2008.
11. **Lai SK, Wang YY, Wirtz D, Hanes J.** Micro- and macrorheology of mucus. *Adv Drug Deliv Rev* 61: 86–100, 2009.
12. **Lee WL, Jayathilake PG, Tan Z, Le DV, Lee HP, Khoo BC.** Mucociliary transport: effect of mucus viscosity, cilia beat frequency and cilia density. *Comput Fluids* 49: 214–221, 2011.
13. **Lima R, Ishikawa T, Imai Y, Takeda M, Wada S, Yamaguchi T.** Measurement of individual red blood cell motions under high hematocrit

conditions using a confocal micro-PTV system. *Ann Biomed Eng* 37: 1546–1559, 2009.
14. **Lucas AM, Douglas LC.** Principles underlying ciliary activity in the respiratory tract. II. A comparison of nasal clearance in man, monkey and other mammals. *Arch Otolaryngol Head Neck Surg* 20: 255–264, 1934.
15. **Matsui H, Randell SH, Peretti SW, Davis W, Boucher RC.** Coordinated clearance of periciliary liquid and mucus from airway surfaces. *J Clin Invest* 102: 1125–1131, 1998.
16. **Nigg EA, Raff JW.** Centrioles, centrosomes, and cilia in health and disease. *Cell* 139: 663–678, 2009.
17. **Nonaka S, Tanaka Y, Okada Y, Takeda S, Harada A, Kanai Y, Kido M, Hirokawa N.** Randomization of left-right asymmetry due to loss of nodal cilia generating leftward flow of extraembryonic fluid in mice lacking KIF3B motor protein. *Cell* 95: 829–837, 1998.
18. **Okada Y, Nonaka S, Tanaka Y, Saijoh Y, Hamada H, Hirokawa N.** Abnormal nodal flow precedes situs inversus in *iv* and *INV* mutant mice. *Mol Cell* 4: 459–468, 1999.
19. **Pazour GJ, Dickert BL, Vucica Y, Seeley ES, Rosenbaum JL, Witman GB, Cole DG.** *Chlamydomonas* IFT88 and its mouse homologue, polycystic kidney disease gene tg737, are required for assembly of cilia and flagella. *J Cell Biol* 151: 709–718, 2000.
20. **Ryser M, Burn A, Wessel TH, Frenz M, Ricka J.** Functional imaging of mucociliary phenomena. *Eur Biophys J* 37: 35–54, 2007.
21. **Saadatmand M, Ishikawa T, Matsuki N, Abdekhodaie MJ, Imai Y, Ueno H, Yamaguchi T.** Fluid particle diffusion through high-hematocrit blood flow within a capillary tube. *J Biomech* 44: 170–175, 2011.
22. **Sanderson MJ, Sleigh MA.** Ciliary activity of cultured rabbit tracheal epithelium: beat pattern and metachrony. *J Cell Sci* 47: 331–347, 1981.
23. **Smith DJ, Gaffney EA, Blake JR.** Modelling mucociliary clearance. *Respir Physiol Neurobiol* 163: 178–188, 2008.
24. **Smith DJ, Gaffney EA, Blake JR.** A viscoelastic traction layer model of mucociliary transport. *Bull Math Biol* 69: 289–327, 2007.
25. **Smith DJ, Gaffney EA, Blake JR.** A model of tracer transport in airway surface liquid. *Bull Math Biol* 69: 817–836, 2007.
26. **Smith DJ, Gaffney EA, Blake JR.** Discrete cilia modeling with singularity distributions: application to the embryonic node and the airway surface liquid. *Bull Math Biol* 69: 1477–1510, 2007.
27. **Ueno H, Ishikawa T, Bui KH, Gonda K, Ishikawa T, Yamaguchi T.** Mouse respiratory cilia with the asymmetric axonemal structure on sparsely distributed ciliary cells can generate overall directional flow. *Nanobio Nanotechnol* 8: 1081–1087, 2012.
28. **Yi WJ, Park KS, Lee CH, Rhee CS.** Correlation between ciliary beat frequency and metachronal wave disorder using image analysis method. *Med Biol Eng Comput* 41: 481–485, 2003.

254

# FEBS Letters

ELSEVIER
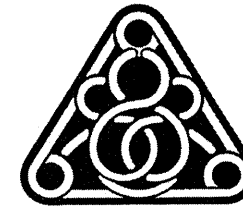
# Expression, phosphorylation and function of the Rab-GTPase activating protein TBC1D1 in pancreatic beta-cells

CrossMark

Sabine Rütti [a,*], Caroline Arous [a], Alexandra C. Nica [a], Makoto Kanzaki [b], Philippe A. Halban [a], Karim Bouzakri [a]

[a] Department of Genetic Medicine and Development, University Medical Center, University of Geneva, Geneva, Switzerland
[b] Department of Biomedical Engineering, Graduate School of Biomedical Engineering, Tohoku University, Japan

## ARTICLE INFO

## ABSTRACT

The Rab-GTPase activating protein TBC1D1 is a paralog of AS160/TBC1D4. AS160/TBC1D4, a downstream effector of Akt, has been shown to play a central role in beta-cell function and survival. The two proteins have overlapping function in insulin signalling in muscle cells. However, the expression and the potential role of TBC1D1 in beta-cells remain unknown. Therefore, the aim of this study is to investigate whether TBC1D1 is expressed in beta-cells and whether it plays, as AS160/TBC1D4, a role in beta-cell function and survival. Using human and rat beta-cells, this study shows for the first time that TBC1D1 is expressed and phosphorylated in response to glucose in these cells. Knockdown of TBC1D1 in beta-cells resulted in increased basal and glucose-stimulated insulin release, decreased proliferation but no change in apoptosis.

Structured summary of protein interactions:
TBC1D1, glucagon and insulin colocalize by fluorescence microscopy (View interaction)

## 1. Introduction

The mechanism and the signalling pathways that regulate insulin secretion and beta-cell mass represent a critical issue for understanding diabetes mellitus, a disease characterized in its two major forms by a relative or absolute deficiency in the number of pancreatic beta-cells. Studies that involved insulinoma cells and animal models with genetic knockout of the insulin receptor, insulin receptor substrates, and insulin-like growth factor I receptor (IGFIR) provided evidence that insulin/IGFIR/PI3K signalling pathways mediate insulin action in beta-cells [1,2]. Moreover, these studies demonstrated that activation of the insulin receptor and insulin receptor substrate is required for the glucose effects on beta-cell growth and survival. The complexity of insulin signalling cascades is highlighted by the existence of multiple isoforms of target proteins implicated in metabolic and gene-regulatory events. Rab-GTPase activating protein (Rab-GAP) AS160, also known as TBC1D4, is a major downstream effector of insulin signalling in insulin sensitive tissues (muscle and fat) and is implicated in GLUT4 translocation [3].

Recently, we showed that AS160/TBC1D4 is expressed and phosphorylated in response to glucose in pancreatic human beta-cells and is involved in glucose stimulated insulin secretion (GSIS), proliferation and survival [4]. This study revealed that AS160/TBC1D4 plays a central role in beta-cell function and survival, in line with previous studies demonstrating that the insulin signalling pathway plays a central role in beta-cells.

TBC1D1, a paralog of TBC1D4, has been shown to be expressed in human skeletal muscle and to be involved in GLUT4 translocation after insulin stimulation or muscle contraction [5]. Moreover, several studies have demonstrated a critical role for TBC1D1 in glucose and lipid metabolism as well as in whole body energy homeostasis [6]. Nevertheless, a genetic variant of TBC1D1 (R125W) is associated with predisposition for human obesity [7]. There is approximately 50% homology between AS160/TBC1D4 and TBC1D1, but the Rab-GAP domains are almost identical, thus implying that the 2 proteins might have some overlapping function [8]. Indeed, it has been shown that in their non-phosphorylated state AS160/TBC1D4 and its paralog TBC1D1 retain GLUT4 in intracellular vesicles by keeping target Rabs in an inactive, GDP-bound state. When TBC1D1/4 Rab-GAP activity is inhibited by phosphorylation, GLUT4 vesicles are released for translocation to the cell surface, leading to increased transport of glucose across the cell membrane [3]. In skeletal muscle and adipose tissue, insulin treatment and subsequent AMPK activation induce a specific

* Corresponding author. Address: Department of Genetic Medicine and Development, University Medical Center, 1 rue Michel-Servet, 1206 Geneva, Switzerland. Fax: +41 22 379 55 28.
E-mail address: sabine.rutti@unige.ch (S. Rütti).

---

phosphorylation profile of TBC1D1 (Ser-237 and Thr-596). This phosphorylation profile determines its specific activation [9]. Moreover, the presence only on TBC1D1 and not on TBC1D4 of an AMPK dependent site of phosphorylation (Ser-237 in humans and Ser-231 in rats) contributes in part to explain its unique regulatory properties [10]. We and others have demonstrated in the past that a parallel can be made between the regulation of GLUT4 and insulin granule trafficking [1,11].

The aim of the present study was to investigate whether TBC1D1 is expressed and phosphorylated in response to glucose in primary human and rat sorted beta-cells and if so to determine its involvement in GSIS as well as in beta-cell proliferation and survival.

## 2. Methods

### 2.1. Islets, primary beta-cell purification and culture

Islets of Langerhans were isolated by collagenase digestion of pancreas from adult male Wistar rats. This study was conducted and the animal sacrificed with the authorization from Geneva State Veterinarian's Office. Beta-cells were separated from non-beta-cells by autofluorescence-activated cell sorting (FACS) using a FACSVantage (Becton Dickinson, Franklin Lakes, NJ) as described previously [12]. Sorted rat beta-cells purity was assessed by immunofluorescence staining for insulin. Sorted rat beta-cells were cultured in DMEM medium containing 11 mmol/l glucose, 0.05 mg/ml gentamicin, 100 U/ml penicillin, 100 mg/ml streptomycin, and 10% fetal calf serum (Sigma–Aldrich, St. Louis, MO, USA). Sorted rat beta-cells were cultured on plastic dishes coated with extracellular matrix derived from 804G cells as described elsewhere [12] and were left for 24 h to adhere and spread before initiation of the experiments.

Human islets were kindly provided by the Cell Isolation and Transplant Centre of the University of Geneva, through JDRF award 31-2008-413 (ECIT Islet for Basic Research Program). Human islets were dispersed by Acutase (PAA Laboratories, Pasching, Austria) and beta-cells were sorted by FACS after labelling with Newport Green and exclusion of ductal cells and dead cells using a FACSVantage (Becton Dickinson) as described before [12]. The purity of the beta-cells was performed for each preparation using immunofluorescence staining for insulin and glucagon.

### 2.2. RNA interference mediated knockdown of endogenous TBC1D1 by transient transfection

Knockdown of TBC1D1 in rat primary beta-cells was achieved by transfection with specific small interfering RNA (Tbc1d1RSS323178(3_RNAI) + Tbc1d1RSS323179(3_RNAI) + Tbc1d1RSS323180(3_RNAI) from Invitrogen, Life Technologies, Grand Island, NY, USA) and control siRNA (SignalSilence Control siRNA, Cell Signaling Technology, Danvers, MA, USA) using a method described previously [13]. In brief, liposome–siRNA (Lipofectamine 2000 from Life Technologies and 100 nM siRNA) was prepared in 200 μl opti–Modified Eagle's Medium as described by the suppliers (Life Technologies).

### 2.3. RNA extraction, library preparation, sequencing and read mapping

Sorted beta-cells and islets were centrifuged, the supernatant was removed and the pellet disrupted in RLT buffer (RNeasy, Qiagen, Hilden, Germany). Total RNA was prepared according to the standard RNeasy protocol. Total RNA library construction, RNA sequencing and read mapping was performed as described in detail elsewhere [14].

### 2.4. Expression quantification

GENCODE annotation v10 was used to assign filtered reads to their corresponding exons and genes. The gene counts were incremented non-redundantly i.e. reads overlapping two exons are counted once to the total count sum per gene. Resulting raw gene counts were normalized to gene length (sum of exons) and sequencing depth i.e. RPKM – reads per kilobase per million mapped reads [14].

### 2.5. Western blotting

Phosphorylation and expression of TBC1D1, or expression of CDK4, Akt and actin was determined by Western blot analysis. Beta-cell protein lysate was separated by SDS-PAGE, transferred to Immobilon-P membranes (Millipore), and probed with anti-TBC1D1 or anti-pTBC1D1 (Serine 231 and Threonine 596, developed by Makoto Kanzaki) and secondary horseradish peroxidase-conjugated antibodies. Anti-actin was obtained from Merck Millipore, (Zug, Switzerland), anti-CDK4 from Santa Cruz Biotechnology Inc. (Heidelberg, Germany) and anti-Akt from Cell Signaling.

### 2.6. Insulin secretion

For acute insulin release in response to glucose, primary rat beta-cells were washed, preincubated for 2 h (2.8 mmol/l glucose) and incubated in Krebs–Ringer bicarbonate Hepes (KRB) buffer (0.5% BSA) containing 2.8 mmol/l glucose for 1 h followed by 1 h incubation in KRB containing 16.7 mmol/l glucose or by 10 min incubation with KRB containing 30 mM KCl. Islet insulin was extracted with 0.18 M HCl in 70% ethanol for determination of insulin content. Secreted insulin and insulin content were measured by radioimmunoassay using rat insulin standards.

### 2.7. Cell proliferation and death

Sorted rat beta-cells were established in monolayer on dishes coated with 804G-ECM [12]. Two days after transfection, BrdU was added to the cells for 24 h. The incorporated BrdU was detected with an anti-BrdU antibody according to the manufacturer's instructions (BrdU kit; Roche Diagnostics, Rotkreuz, Switzerland) and the beta-cells were co-stained with an anti-insulin antibody. The free 3-OH strand breaks resulting from DNA degradation were detected by the terminal deoxynucleotidyl-transferase-mediated deoxyuridine 5-triphosphate nick-end labeling (TUNEL) technique according to the manufacturer's instructions (in situ cell death detection kit; Roche Diagnostics). The beta-cells were co-stained with an anti-insulin antibody. The numbers of proliferative or apoptotic cells were determined using a fluorescent microscope. For each condition in each individual experiment, over 1000 cells were analyzed.

### 2.8. Immunofluorescence

TBC1D1 and phospho-TBC1D1 were detected with specific anti-TBC1D1, anti-phospho-TBC1D1-Ser-231/237 and anti-phospho-TBC1D1-Thr-596 antibodies developed by us (Dr. Makoto Kanzaki) according to standard procedures for fixation and confocal fluorescence microscopic observation. Beta- and alpha-cells were identified by insulin and glucagon immunofluorescence respectively.

### 2.9. Statistical analyses

Data are expressed as means ± S.E.M., with the number of individual experiments presented in the figure legends. All data were tested for normality and analyzed with/ PRISM (GraphPad,

San Diego, CA, USA). Differences were evaluated using Student's t test and ANOVA with Bonferroni post hoc test for multiple comparison analysis. Significance was set as P < 0.05.

## 3. Results

### 3.1. TBC1D1 is expressed in pancreatic islets and primary beta-cells and is phosphorylated in response to glucose

TBC1D1 is a paralog of TBC1D4 and like it, is phosphorylated in response to insulin in skeletal muscle and adipocytes [3,15]. Using RNA sequencing, we report for the first time that TBC1D1 is expressed at the mRNA level in human islets and also in FACS-sorted primary human beta-cells (86.7 ± 6.8% insulin positive cells). With this technique, the number of mRNA copies for each gene was obtained, allowing to directly compare the expression of genes of interest. We observed that the expression of TBC1D1 was lower than AS160/TBC1D4 in human sorted beta-cells but similar for the 2 isoforms in human islets (Fig. 1A). Moreover, we observed in dispersed human islet cells co-stained for TBC1D1 (red), insulin (green) and glucagon (cyan) that TBC1D1 co-localizes with both glucagon and insulin (Fig. 1B). These immunofluorescence results confirm that TBC1D1 is expressed at the protein level in both these human islets cell types.

We use a silencing approach in order to study the role of TBC1D1 in beta-cells. However, in our hands siRNA transfection of human beta-cells is not feasible. Therefore we used primary rat beta-cells for this purpose, having shown previously that siRNA transfection is efficient in these cells [4,13]. We analysed TBC1D1 protein expression and phosphorylation in rat primary sorted

beta-cells (over 90% insulin positive cells) by immunofluorescence (Fig. 1C). We investigated the phosphorylation of 2 key sites on rat TBC1D1: Thr-596 and Ser-231. TBC1D1 Thr-596 is a phosphorylation site identical to Thr-642 on AS160/TBC1D4. We have observed that AS160/TBC1D4 Thr-642 is phosphorylated in response to glucose in beta cells and that this phosphorylation is Akt dependent (unpublished observation). TBC1D1 Ser-231 is the rat phosphorylation site equivalent to human Ser-237, a motif recognized by AMPK that has been shown to be phosphorylated in muscle after exercise and to be involved in Glut4 trafficking [9]. TBC1D1 Ser-231 is phosphorylated in rat beta-cells already after 10 min glucose stimulation (Fig. 2A) and this phosphorylation is still present after 60 min glucose stimulation (Figs. 1C and 2B). By contrast, 10 min glucose stimulation is not sufficient to induce TBC1D1 Thr-596 phosphorylation (Fig. 2C) whereas this site is phosphorylated after 60 min glucose stimulation (Figs. 1C and 2D). Taken together, these data on TBC1D1 expression and phosphorylation after glucose stimulation suggest that this protein might play a role in beta-cell response to glucose.

### 3.2. Modulation of beta-cell function and proliferation by TBC1D1 silencing

To study the biological function of TBC1D1, primary rat beta-cells were transfected with siRNA against TBC1D1 or scrambled siRNA (control). Cells transfected with TBC1D1 siRNA showed a 70% reduction in TBC1D1 protein expression (Fig. 3A). In cells with such reduced TBC1D1 expression, basal insulin as well as glucose stimulated insulin secretion were modestly increased without any change in fold-stimulation (Fig. 3B) and total insulin content
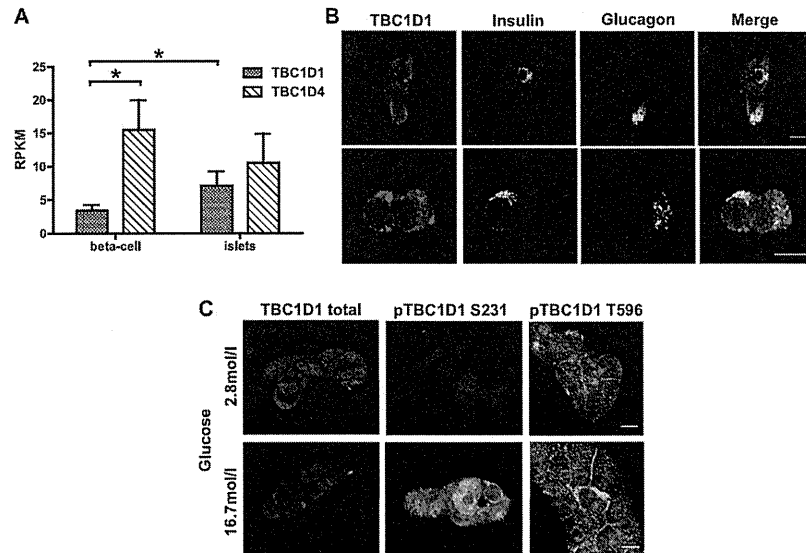
Fig. 1. TBC1D1 expression and phosphorylation. (A) TBC1D1 and AS160/TBC1D4 mRNA expression in human islets (n = 11) and sorted beta-cells (n = 6) presented as reads per kilobase per million mapped reads (RPKM). *P < 0.05 as tested by ANOVA followed by Bonferroni post hoc test. (B) Representative images of dispersed islet cells co-stained for TBC1D1 (red), insulin (green), glucagon (cyan) and nucleus (blue). (C) Representative images of primary rat sorted beta-cells co-stained for TBC1D, phosphorylated TBC1D1 Ser-231 or phosphorylated TBC1D1 Thr-596 (green) and DAPI (blue) under basal conditions (2.8 mmol/l glucose) or after 60 min stimulation with 16.7 mmol/l glucose. Scale bar: 10 μm.
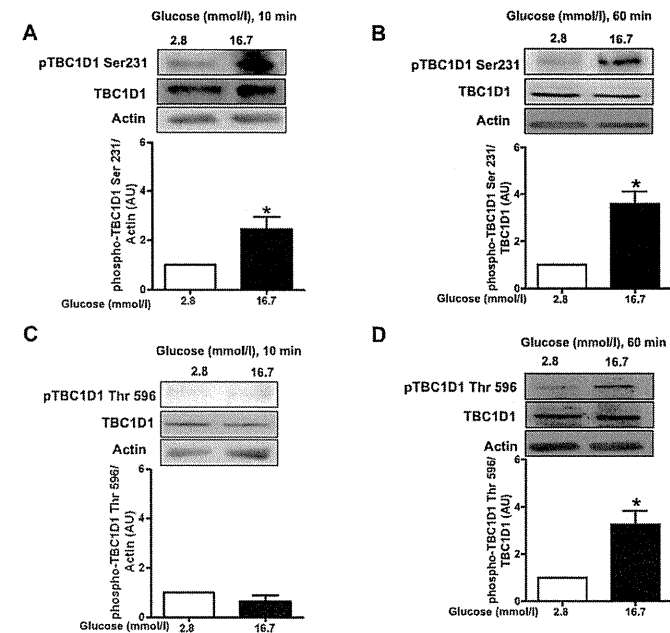
Fig. 2. TBC1D1 phosphorylation in response to glucose. (A) Representative Western blot and quantification of TBC1D1 Ser-231 phosphorylation in primary rat beta-cells at 2.8 mmol/l glucose (open bars) or after 10 min stimulation with 16.7 mmol/l glucose (closed bars) (n = 3). (B) Representative Western blot and quantification of TBC1D1 Ser-231 phosphorylation in primary rat beta-cells at 2.8 mmol/l glucose (open bars) or after 60 min stimulation with 16.7 mmol/l glucose (closed bars) (n = 3). (C) Representative Western blot and quantification of TBC1D1 Thr-596 phosphorylation in primary rat beta-cells at 2.8 mmol/l glucose (open bars) or after 10 min stimulation with 16.7 mmol/l glucose (closed bars) (n = 4). (D) Representative Western blot and quantification of TBC1D1 Thr-596 phosphorylation in primary rat beta-cells at 2.8 mmol/l glucose (open bars) or after 60 min stimulation with 16.7 mmol/l glucose (closed bars) (n = 4). *P < 0.05 vs 2.8 mmol/l glucose by Student's t test.

(data not shown). These results suggest that TBC1D1 is not essential for GSIS in sorted rat primary beta-cells, in marked contrast to our earlier results documenting a direct role of AS160/TBC1D4 in this process [4]. We also stimulated the beta-cells with KCl which induces calcium influx and thereby insulin secretion independently of glucose metabolism. Knockdown of TBC1D1 totally prevented KCl induced insulin secretion (Fig. 3C).

To investigate the impact of TBC1D1 silencing on rat primary beta-cell apoptosis and proliferation in culture, cell death was quantified using TUNEL assay and cell replication was assessed by BrdU incorporation over 24 h. Knockdown of TBC1D1 did not affect beta-cell death (Fig. 4A and B). However, proliferation of primary rat beta-cells transfected with TBC1D1 was dramatically decreased when compared to cells transfected with scrambled siRNA (Fig. 4C). This marked reduction in proliferation when TBC1D1 is knocked down was also observed with elevated glucose concentrations in the rat beta-cell culture media (22 mM or 33 mM glucose, data not shown). We also investigated the expression of 2 proteins implicated in beta-cell survival and proliferation, Akt and Cdk4; neither was influenced by TBC1D1 knockdown.

## 4. Discussion

We have recently demonstrated that TBC1D4/AS160 is expressed in human and rodent pancreatic beta-cells and

phosphorylated after glucose stimulation [4]. We further established that this protein is involved in glucose induced insulin secretion, proliferation and survival of primary sorted beta-cells [4]. TBC1D1 and AS160/TBC1D4 have significant sequence similarity and overlapping function in insulin responsive tissues [8]. Nevertheless, the presence only on TBC1D1 and not on TBC1D4 of an AMPK dependent site of phosphorylation on Ser-231 in the rat protein studied here (corresponding to Ser-237 in the human protein) may contribute towards its unique regulatory properties [10]. In the present study, we reveal for the first time that TBC1D1 is expressed and phosphorylated upon glucose stimulation in human islets, as well as in human and rat isolated beta-cells. Quantification of mRNA levels by RNA sequencing indicates that TBC1D1 is less abundant than TBC1D4/AS160 in beta-cells but comparable in islets. The higher levels of TBC1D1 mRNA in islets than beta-cells suggest relatively greater expression in islet non-beta-cells (composed of approximately 60% alpha-cells) or in exocrine cells that might contaminate human islet preparations. Our results were supported by immunofluorescence staining of dispersed human islet cells where we observed the expression of TBC1D1 at the protein level in beta- as well as alpha-cells.

Since TBC1D1 is expressed and phosphorylated in response to glucose in rat primary beta-cells, we have used these cells to study the role of TBC1D1 in beta-cell function, proliferation and survival. Several studies have shown that a parallel mechanism could be